

Department of Physics and Astronomy
University of Heidelberg

Master thesis

in Physics

submitted by

Matteo Zortea

born in Borgo Valsugana (Italy)

2023

Investigating a Yukawa Theory
with Coloured Stochastic Quantisation

This Master thesis has been carried out by Matteo Zortea

at the

Institute for Theoretical Physics, Heidelberg

under the supervision of

Prof. Dr. Jan M. Pawłowski

and

Dr. Felipe Attanasio

Investigating a Yukawa Theory with Coloured Stochastic Quantisation

Stochastic quantisation with coloured noise allows for explicit control of the momentum dependency of quantum fluctuations in a quantum field theory. In this thesis, the technique is implemented via a Langevin Monte Carlo algorithm to investigate a two flavours Yukawa model. Applications include studying the fluctuations content of the theory, noise-induced phase transitions, and cooling the simulation by systematically removing ultraviolet degrees of freedom, in connection with the Kadanoff-Wilson renormalisation group.

Anwendung von Farbiger Stochastischer Quantisierung auf eine Yukawa-Theorie

Stochastische Quantisierung mit farbigem Rauschen ermöglicht eine explizite Kontrolle der Impulsabhängigkeit der Quantenfluktuationen einer Quantenfeldtheorie. In dieser Arbeit wird diese Technik im Rahmen eines Langevin Monte Carlo Algorithmus implementiert, um ein Yukawa-Modell mit zwei Flavours zu untersuchen. Dabei werden zunächst der Rauschanteil der Theorie und durch das Rauschen induzierte Phasenübergänge untersucht, es folgt das Kühlen der Simulation durch systematisches Entfernen ultravioletter Freiheitsgrade in Verbindung mit der Kadanoff-Wilson-Renomierungsgruppe.

Contents

1	Introduction and outline	1
1.1	Quantum chromodynamics and its phase diagram	1
1.2	Lattice Field Theory	2
1.3	The emergence of effective theories	3
1.4	Outline	4
2	Theoretical background	5
2.1	The renormalisation group	5
2.1.1	Block-spin RG	5
2.1.2	Wilsonian RG	7
2.2	Lattice QFT and the continuum limit	9
2.3	Stochastic quantisation	11
2.3.1	Standard stochastic quantisation	11
2.3.2	Stochastic quantisation with coloured noise	12
2.4	Chiral symmetry	14
2.4.1	Chiral symmetry in the continuum	14
2.4.2	Chiral symmetry on the lattice	16
2.5	Yukawa theory	16
2.5.1	Description of the model	16
2.5.2	Chiral symmetry in the Yukawa model	17
3	Methods and algorithms	19
3.1	Discretisation of the Yukawa theory	19
3.2	Langevin Monte Carlo	21
3.3	Applications of coloured noise in lattice QFT	22
3.3.1	Classical-to-quantum interpolation	22
3.3.2	Noise-induced transition	22
3.3.3	Cooling and the continuum limit of effective theories	23
3.3.4	Control over temperature	24
3.4	Definition of relevant observables	25
4	Numerical investigation: preliminaries	31
4.1	Inversion of the Dirac operator	31
4.2	The fermionic correlator	32
4.3	Phase structure of the Yukawa theory	37
5	Numerical investigation: coloured noise	41
5.1	Classical-to-quantum interpolation	41
5.2	Chiral fermions and noise-induced transition	43
5.3	Cooling with coloured noise	46
6	Summary and outlook	51

Acknowledgements	53
A Conventions	55
B Wilson fermions	57
C Computational strategies	59
Bibliography	63

Chapter 1

Introduction and outline

1.1 Quantum chromodynamics and its phase diagram

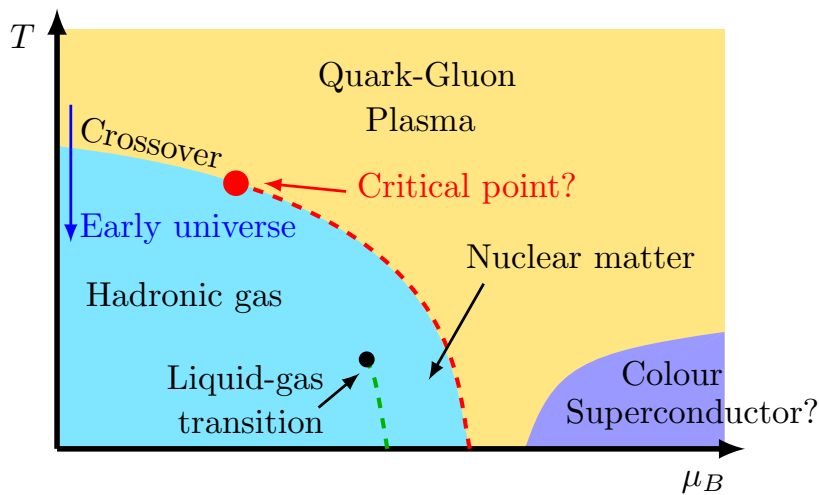


FIGURE 1.1: Conjectured phase diagram of Quantum Chromodynamics. At low temperature and chemical potential, Quantum Chromodynamics exists in a chirally broken state, where quarks and gluons are confined into hadrons and cannot be observed as single particles. As temperature or chemical potential are raised above a critical threshold, chiral symmetry is restored and particles lie in a quark-gluon plasma state. The existence and location of the critical point, as well as the colour superconducting state, is still matter of ongoing research.

Quantum Chromodynamics (QCD) plays a fundamental role in our understanding of the Standard Model. It is the theory describing the strong force among quarks, gluons and the composition of hadrons such as protons and neutrons, which constitutes the base of most of the matter around us.

The diagram reported in Figure 1.1 illustrates the phases of QCD as a function of temperature (T) and baryon chemical potential (μ_B). At low temperature and chemical potential, QCD exhibits confinement [1, 2], a phenomenon for which only colour-neutral states can be observed. The confined phase is characterised by a spontaneously broken chiral symmetry, while the restoration of chiral symmetry is expected in the transition towards a quark-gluon plasma at high temperatures (roughly $T > 160$ MeV) or chemical potential (roughly $\mu_B > 1$ GeV) [3–7]. Moreover, also new states of matter are hypothesized, such as the existence of the colour superconducting state [8–10].

Much more has to be studied in the phase diagram, such as the precise determination of the location and nature of the critical point (if it exists at all). It's a huge challenge that needs a combination of theory, experiments, and simulations.

On the theoretical side, a wide number of results have been obtained from functional methods such as the functional renormalisation group and (fRG) and Dyson-Schwinger equations (DSE) [11–13]. The major experiments are performed at the Relativistic Heavy Ion Collider (RHIC) in New York and the Large Hadron Collider (LHC) at CERN. The Facility for Antiproton and Ion Research (FAIR) in Darmstadt, Germany, is a new collider under construction. On the simulation side, lattice field theory has become the standard approach to study QCD and particle physics and a large number of results have been obtained [7, 14–16].

For a more detailed overview of the features of the QCD phase diagram see [17, 18].

1.2 Lattice Field Theory

Computing physical quantities from first principle approaches is not only hard to do, but results often impossible since a naïve approach yields diverging results. In fact, most quantum field theories need to be regularised by introducing an ultraviolet cutoff. To do this, one often relies on expansion techniques such as perturbation theory, in which one tries to regularise the theory order by order in an expansion on the interaction coupling, yielding finite quantities that depend on the truncation order. While this method is capable of producing incredibly precise results, it fails completely in treating non-perturbative phenomena, namely effects that cannot be captured by any order in the expansion or that are typical of strongly interacting systems. Phenomena such as confinement are non-perturbative.

A standard formulation of quantum field theory is also not very suitable for numerical computations since the path integral measure and the action are infinite dimensional objects.

Lattice field theory [19–22], which was proposed by Kenneth G. Wilson in 1974 [23], is meant at first as a powerful non-perturbative regularisation tool to prevent divergences to occur and render the computation of the correlation functions finite. Moreover, it also provides a framework to study quantum field theory numerically on a computer. In order to accomplish this, one defines the theory on a spacetime lattice and makes use of statistical methods such as Monte Carlo algorithms to compute observables. One should not view the lattice as an approximation to the continuum theory. It rather defines a theory that is undefined directly in the continuum [24]. One may then wonder how can one reconstruct a result in the continuum theory, keeping the results finite, and matching the results on the discretised theory to physically measured ones. This task, far from being simple, will be discussed in the next chapters.

Lattice QCD does not come without problems. Simulations at large chemical potential are in fact hard due to the presence of the sign problem. Amongst other candidates, a promising method aimed at solving the issue is Stochastic Quantisation based on the Complex Langevin equation [25–28]. In fact, it successfully produced a wide number of results in studying the phase diagram of QCD and similar theories [29–33]. For a review of the method, we refer to [34, 35]. Here, we just want to mention that convergence of the Complex Langevin algorithm often requires gauge cooling techniques [36] that remove configurations with large ultraviolet fluctuations. In this sense, the cooling technique that will be presented in this work could be of great benefit to the algorithm.

1.3 The emergence of effective theories

A central role in our investigation will be played by the Wilsonian perspective of the Renormalization Group (RG) [37–39]. Within this paradigm, renormalization ceases to be merely a tool for taming divergences; the Wilsonian RG approach provides a rigorous way to perform a change of scale in a physical theory. The Wilson framework naturally brings to the concept of effective theory, a model where irrelevant degrees of freedom are averaged out and replaced by an effective description in terms of the relevant quantities at the given scale.

Effective theories are widely used to study QCD, aiming at tailoring to specific aspects of the strong force dynamics. Among others, we mention the Nambu – Jona-Lasinio model [40, 41], the Gross-Neveu model [42], and the Quark-Meson model [43–45]. All of these theories are Yukawa-type theories, namely theories that can be described in terms of a fermion-boson-fermion interaction. This fact motivates the choice of the model in our work.

1.4 Outline

Chapter 2 is devoted to the introduction of the theoretical background that supports this work.

We will start with the Kadanoff and Wilson approach to renormalisation in statistical physics and quantum field theory. Lattice field theory is then introduced as a powerful tool to simulate quantum field theory numerically and the basics of the formulation are provided. We then turn to stochastic quantisation, the relation between noise and quantum fluctuations, and how the standard formulation is modified by the presence of coloured noise. This results in a deep connection between coloured stochastic quantisation and the renormalisation group. We then turn to the discussion of chiral symmetry and its breaking, both in the continuum and on the lattice. The chapter ends with a description of the model on which the above techniques are applied, namely a Yukawa theory.

Chapter 3 is devoted to detail techniques and methodologies of the project.

We will start by explaining how the continuum model is discretised on a spacetime lattice and how it can be simulated via a Monte Carlo method based on stochastic quantisation. Some possible applications of coloured noise in lattice QFT are then listed, and the numerical experiments that are carried out in the last chapter are described. The chapter ends with a description of the relevant observables that are employed to study a lattice quantum field theory.

Chapters 4 and 5 are devoted to the numerical investigation.

First, some preliminary analysis is carried out. The procedure of extracting fermionic masses in the simulation is illustrated, and a panoramic view over the general phase structure of the theory is provided. The latter will guide the choice of parameter settings for all the simulations. It is then shown how coloured noise can be used to provide a smooth interpolation between the fully classical and fully quantum pictures. The introduction of noise can cause a qualitative change in the behaviour of the system. In particular, it is shown how it can trigger a phase transition in the model. Finally, the connection with the Kadanoff-Wilson RG is exploited to cool a simulation by systematically encoding ultraviolet (UV) fluctuations in a redefinition of the classical action, without altering the physical content of the theory.

Chapter 2

Theoretical background

In this chapter we want to provide an overview over the general theoretical framework that supports this work and introduce the main concepts for the successive parts. Each section in this chapter is, by no means, meant as an exhaustive treatment. The description will be quite conceptual, rather than technical, and aims at recalling the main ideas and fixing conventions. We ask the reader to consult appropriate references, which will be given in the corresponding sections, for a more detailed treatment of the topics.

2.1 The renormalisation group

Landau's mean-field approach to study phase transition [46] gained wide popularity in the 1930's and 40's, since it was able to describe critical properties of many systems and it provided inspiration for the later Landau-Ginzburg theory of superconductivity [47]. Thus, it was soon proved to be inaccurate to predict experimentally well proven properties of systems near their critical point [37, 48], such as, for example, the Kondo problem [49]. This is because, being a mean field theory, it did not take into account the role of spatial fluctuations. The idea of block-spin transformation, systematically developed by Kadanoff [50], made a big step towards a deeper understanding of the scaling behaviour, and formed the basis for the later works of Wilson [37, 38, 51], which still constitutes the basis for modern approaches to renormalisation in field theory and statistical physics.

2.1.1 Block-spin RG

To illustrate the idea, let us consider a set of spins whose magnetisation is described by a function $\phi(x)$. The spins are located on a discrete lattice \mathcal{L} with spacing a , so that the function assumes values only at such sites $\phi(x_i) = \phi_i \neq 0 \Leftrightarrow x_i \in \mathcal{L}$. Suppose then that their interaction is described by a certain action $S[\phi]$ and a partition function

$$Z = \sum_{\{\phi\}} e^{-S[\phi]},$$

where the sum is performed over the possible configurations of the field ϕ .

We now want to introduce a coarse-grained (or blocked) field $\bar{\phi}$ within a spacetime cell of volume \mathcal{V} . Such a coarse-grained field can be defined, for example, as an average over the spins within the cell \mathcal{V} . If the spins can only be 0 or 1 like in the Ising model, then we might opt for a majority rule [52].

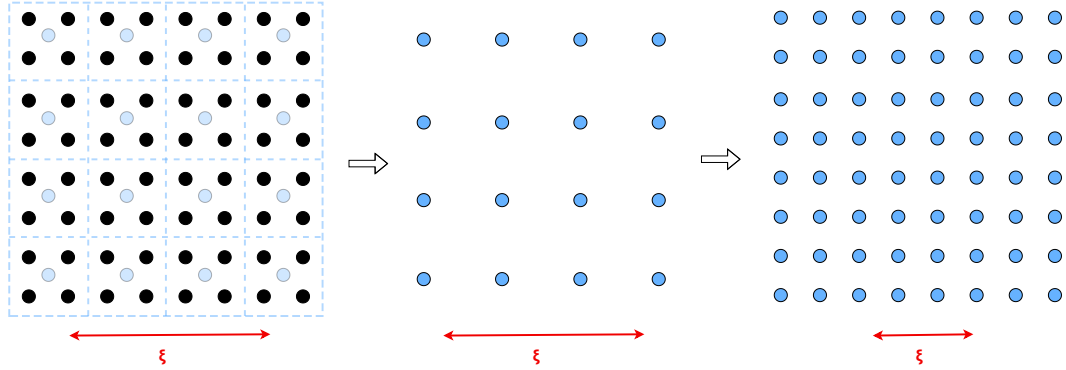


FIGURE 2.1: The two steps of the block-spin transformation. The black dots indicate the original field ϕ , while the blue dots indicate the coarse-grained field $\bar{\phi}$.

We now want to find a new action S_b such that

$$Z = \sum_{\phi} e^{-S(\phi)} = \sum_{\bar{\phi}} e^{-S_b(\bar{\phi})}. \quad (2.1)$$

Suppose for the moment that such S_b has been found. The coarse-graining procedure comes with a loss of resolution since the spacing is changed $a \rightarrow 2a$. Hence one can rescale distances and momenta in the new action via $a \rightarrow a/2$, $p \rightarrow 2p$ and then compare the result with the initial action. This constitutes the second step of the block-spin transformation.

The whole procedure can be iterated multiple times, and can be thought as a zoom-out with a corresponding coarse-graining, in order to describe the system in terms of the relevant scales as pictured in Figure 2.1.

An important quantity is the so called correlation length ξ , which gives the length scale of exponential decays of correlation functions between local observables measured at different points on the lattice. As made clear in the picture, the physical correlation length ξ is reduced by the block-spin step since the description is now in terms of the coarse field $\bar{\phi}$. There are only two exceptions for this, either the correlation length is zero, or infinite. In the latter case the system exhibits scale invariance and it is in a fixed point of the RG.

Note that the condition (2.1) is non-trivial. One can, in principle, build an ad-hoc action that fulfills the condition, but it is complicated, since S_b can also be very different from S . For example, if the action $S[\phi]$ contains only nearest-neighbour interactions, the new action $S'[\bar{\phi}]$ can contain higher order interactions such as next-to-nearest neighbour, or even more. In principle, all the terms compatible with the original

symmetries are allowed, and one has often to rely on some approximations. For example, if one is interested in long-range properties of the system, and the volume \mathcal{V} is sufficiently small, one can assume the functional form of the action S to remain approximately the same, with the only change due to the dimensional rescaling of dimensionful quantities mentioned above. Thus, as the procedure is iterated and the correlation length scale is approached, one has to take account higher order interactions. For an example of the explicit construction of the RG for an Ising model, see [52].

2.1.2 Wilsonian RG

The Wilsonian picture of renormalisation [37, 38] is formulated in momentum space and in general is more suitable for theories in the continuum.

The idea is that a physical theory observed at an energy scale Λ can be seen as an effective theory of a more fundamental one, defined at scale $\Lambda_0 > \Lambda$.

To see how this can happen, let us consider a theory defined by the action $S[\phi]$ scale Λ_0 , and let us split the field as

$$\phi = \bar{\phi} + \varphi$$

where $\bar{\phi}$ are fields with momenta $p^2 \leq \Lambda^2$ and φ are fields with $\Lambda^2 < p^2 \leq \Lambda_0^2$.

This allows to split the action as

$$S[\bar{\phi} + \varphi] = S_\Lambda[\bar{\phi}] + \delta S[\bar{\phi}, \varphi],$$

including all the dependence on φ in $\delta S[\bar{\phi}, \varphi]$.

The path integral can be rewritten as

$$\begin{aligned} Z &= \int D\phi e^{-S[\phi]} = \int D\bar{\phi}_\Lambda e^{-S_\Lambda[\bar{\phi}]} \int D\varphi e^{-\delta S[\bar{\phi}, \varphi]} \\ &= \int D\bar{\phi}_\Lambda e^{-S_\Lambda[\bar{\phi}] - S_{\text{UV}}[\bar{\phi}]} \\ &= \int D\bar{\phi}_\Lambda e^{-S_\Lambda^{\text{eff}}[\bar{\phi}]}, \end{aligned}$$

where

$$S_\Lambda^{\text{eff}} = S_\Lambda[\bar{\phi}] + S_{\text{UV}}[\bar{\phi}], \quad S_{\text{UV}}[\bar{\phi}] = -\log \left(\int D\varphi e^{-S_\Lambda[\bar{\phi}, \varphi]} \right).$$

$S_{\text{UV}}[\bar{\phi}]$ encodes all the information of UV modes with $\Lambda^2 < p^2 \leq \Lambda_0^2$.

The action $S_\Lambda[\bar{\phi}]$ has the same functional form as the initial action $S[\phi]$, but it is now defined only for fields with momenta $p^2 \leq \Lambda^2$. Instead, $S_\Lambda^{\text{eff}}[\bar{\phi}]$ constitutes an effective description of the original theory at scale Λ and depends only on degrees of freedom with $p^2 \leq \Lambda^2$.

One can then operate a rescaling of distances and momenta to complete the Wilson RG step, according to the parameter

$$s^2 = \Lambda^2 / \Lambda_0^2.$$

If, for example, d_g is the energy dimension of a coupling g in the action, then the rescaling transformation causes

$$g \rightarrow s^{d_g} g.$$



FIGURE 2.2: The Wilsonian perspective of the renormalisation group. Microscopic degrees of freedom stemming from ultraviolet quantum fluctuations above the scale Λ are averaged out and effectively encoded in the coarse-grained action S_{Λ}^{eff} .

The same applies to the fields and other dimensionful quantities. If the corrections from S_{UV} are negligible, such as for high cutoff $\Lambda \approx \Lambda_0$, then this is the only contribution to the change in the couplings and fields due to the Wilson step. More in general, for higher order iterations of the procedure, the couplings' dependence on s is captured by the β -functions

$$\beta_g = \frac{d}{ds} g(s).$$

A full treatment of RG is out of scope here and we ask the reader to consult more appropriate references for more details [53].

At this point, one can clearly see the analogy with the block-spin transformation introduced in the previous section. Performing the integral over high momenta modes can be thought of as performing averages (coarse-graining) over neighbours. This causes a loss of resolution which can be recovered by rescaling distances and momenta. The rescaling is essential for a description of fixed points since it can be pictured as a zoom-out.

Therefore, the philosophy of Kadanoff and Wilson approaches was that the blocking transformation reduces the complexity of many-body systems by systematically reducing the number of degrees of freedom being taken into account, without changing the physical content of the theory [39, 54].

We want to conclude this section by mentioning that the splitting of the action can be done by writing

$$S_{\Lambda}^{\text{eff}}[\bar{\phi}] = S[\phi] + \Delta S_{\Lambda}[\bar{\phi}],$$

where $\Delta S_{\Lambda}[\bar{\phi}]$ is a regulating function which typically assumes the form

$$\Delta S_{\Lambda}[\bar{\phi}] = \frac{1}{2} \int \frac{d^d p}{(2\pi)^d} \bar{\phi}(-p) \Lambda^2 \left(\frac{1}{r_{\Lambda}(p^2)} - 1 \right) \bar{\phi}(p). \quad (2.2)$$

For a sharp momentum cutoff one has

$$r_{\Lambda}(p^2) = \theta(p^2 - \Lambda^2).$$

This result will allow for a deep connection between coloured stochastic quantisation and the functional renormalisation group [55–59], the latter describing the functional dependence of $S_{\Lambda}^{\text{eff}}[\bar{\phi}]$ on the cutoff scale Λ .

2.2 Lattice QFT and the continuum limit

The starting set up is the Euclidean formulation of quantum field theory, where one typically defines a path integral Z , which, for a general scalar field $\phi(x)$ and a fermion field $\psi(x)$, assumes the form

$$Z = \int \mathcal{D}\phi \mathcal{D}\psi \mathcal{D}\bar{\psi} e^{-S[\phi, \psi, \bar{\psi}]}, \quad \mathcal{D}\xi = \prod_x d\xi_x, \quad \xi \in \{\phi, \psi, \bar{\psi}\}, \quad (2.3)$$

and correlation functions are computed via

$$\langle \xi_{x_1} \dots \xi_{x_n} \rangle = \frac{1}{Z} \int \mathcal{D}\phi \mathcal{D}\psi \mathcal{D}\bar{\psi} \xi_{x_1} \dots \xi_{x_n} e^{-S[\phi, \psi, \bar{\psi}]}, \quad \xi_{x_i} \in \{\phi_{x_i}, \psi_{x_i}, \bar{\psi}_{x_i}\}.$$

Let us then consider a lattice \mathcal{L} , with spacing a , and N_μ points in each spacetime direction μ , hence a physical length $L_\mu = N_\mu a$. For simplicity, we restricted here to a scalar field ϕ and we will recall fermionic properties only when relevant, but what follows has general validity.

The action and the path integral measure are now taken over discrete quantities

$$\begin{aligned} S = \int d^d x \mathcal{L}(\phi(x)) &\rightarrow S = a^d \sum_{n \in \mathcal{L}} \mathcal{L}(\phi(n)), \\ \prod_x d\phi(x) &\rightarrow \prod_{n \in \mathcal{L}} d\phi(n), \end{aligned}$$

where $\mathcal{L}(\phi)$ is the Lagrangian density function.

The path integral is hence

$$Z = \int \prod_n d\phi(n) e^{-S[\phi]},$$

and the probability of a field configuration ϕ is

$$p(\phi) = \frac{1}{Z} e^{-S[\phi]}. \quad (2.4)$$

Expectation values of observables are computed as

$$\langle O(\phi) \rangle = \frac{1}{Z} \int \prod_n d\phi(n) O(\phi) e^{-S[\phi]}. \quad (2.5)$$

In order to simulate a theory and perform the above sums one has to go to a finite volume and impose boundary conditions. In the space directions, we take periodic conditions

$$\begin{aligned} \phi(t, \vec{x}) &= \phi(t, \vec{x} + \vec{T}), \\ \psi(t, \vec{x}) &= \psi(t, \vec{x} + \vec{T}). \end{aligned}$$

A finite time extent is related to the temperature of the system [20, 60] via

$$\beta = 1/T = 1/L_t,$$

and boundary conditions in the time directions are chosen depending on the spin-statistics of the corresponding particles, namely periodic conditions for bosons, and

anti-periodic for fermions

$$\begin{aligned}\phi(t, \vec{x}) &= \phi(t + T, \vec{x}) & \text{bosons,} \\ \psi(t, \vec{x}) &= -\psi(t + T, \vec{x}) & \text{fermions.}\end{aligned}$$

Such a formulation naturally brings a momentum cutoff $\Lambda = \pi/a$ since now all the momenta are restricted to the first Brillouin zone $p_\mu \in [-\pi/a, \pi/a]$.

To compute observables one relies on Monte-Carlo methods to generate field configurations, sampling the distribution (2.4) and convergence to the statistical value given by (2.5) is expected in the limit of infinite samples $N_{\text{samp}} \rightarrow \infty$.

To recover the continuum results, one has to take $V \rightarrow \infty, a \rightarrow 0$ ¹, but this task cannot be done so straightforwardly. Continuum limits of lattice theories are intimately connected to the existence of critical points. To see why this is the case, consider the dimensionless mass gap

$$\hat{\xi} = m a$$

of a certain theory. When taking the continuum limit, we want $a \rightarrow 0$, while having a finite physical mass m . This implies that the correlation length $\hat{\xi}$ has to diverge: in the language of statistical physics, this is a second order phase transition. Of course, to bring the system at its critical point, where such phase transition happens, one has to tune the bare parameters g_0^i of the theory to their critical values g_0^{i*} . To do this, one should find the zeros of the lattice beta functions

$$\beta_g^{\text{latt}} = a \frac{d}{da} g(a) \stackrel{!}{=} 0, \quad a = \pi/\Lambda.$$

As this is quite hard task to do on the lattice, one typically relies on some approximation schemes such as employing perturbative continuum beta functions.

From this description it should emerge that the spacing a should not be treated as a free parameter in the continuum limit, but rather a dynamically determined quantity that depends on the couplings of the theory.

Note that in the limit $a \rightarrow 0$, one has $\Lambda \rightarrow \infty$. If one's scope is to simulate an effective theory which is expected to hold only up to a scale Λ_{phys} , one must have $\Lambda \leq \Lambda_{\text{phys}}$, with a consequent lower bound on the lattice spacing

$$a \geq a_{\text{phys}} = \pi/\Lambda_{\text{phys}}.$$

¹The order here is important, see for example [61, 62]

2.3 Stochastic quantisation

The idea of stochastic quantisation [63, 64] is that Euclidean Quantum Field theory can be thought as a system in thermal equilibrium with a heat reservoir and hence described as a stochastic process via the Langevin equation. For this, one has to introduce a fictitious time variable τ that labels the state $\phi(\tau, x)$ of the system during the evolution.

2.3.1 Standard stochastic quantisation

Let us consider, for example, a scalar field ϕ with a Euclidean action $S[\phi]$ and the following Langevin equation

$$\partial_\tau \phi(\tau, x) = -\frac{\delta S[\phi]}{\delta \phi(\tau, x)} + \eta(\tau, x), \quad (2.6)$$

where $K_\phi(\tau) \equiv -\delta S[\phi]/\delta \phi(\tau, x)$ is the drift term and $\eta(\tau, x)$ is a random white noise field assumed to be normally distributed

$$P(\eta) = \frac{\exp\left(-\frac{1}{4} \int_{\tau, x} \eta^2(\tau, x)\right)}{\int D\eta \exp\left(-\frac{1}{4} \int_{\tau, x} \eta^2(\tau, x)\right)},$$

which, in particular, implies

$$\langle \eta(x, \tau) \rangle = 0, \quad \langle \eta(x, \tau) \eta(x', \tau') \rangle = 2 \delta(x - x') \delta(\tau - \tau'). \quad (2.7)$$

Stochastic average with respect to the measure $P(\eta)$ are computed via

$$\langle A(\eta) \rangle = \int D\eta P(\eta) A(\eta).$$

In momentum space, (2.7) becomes

$$\begin{aligned} \langle \eta(p, \tau) \rangle &= \left\langle \int_x e^{ipx} \eta(x, \tau) \right\rangle = \int_x \langle e^{ipx} \eta(x, \tau) \rangle = 0, \\ \langle \eta(p, \tau) \eta(q, \tau') \rangle &= \left\langle \int_{xy} e^{ipx+iqy} \eta(x, \tau) \eta(y, \tau') \right\rangle \\ &= \int_{xy} e^{ipx+iqy} \langle \eta(x, \tau) \eta(y, \tau') \rangle \\ &= 2 (2\pi)^2 \delta(p + q) \delta(\tau - \tau'). \end{aligned} \quad (2.8)$$

In absence of the noise term $\eta(\tau, x)$, equation (2.6) simply represents an evolution of the field towards the minimum of the action, and at equilibrium the field is constrained to $\partial_\tau \phi(x, \tau) = 0 = \delta S[\phi]/\delta \phi(\tau, x)$, namely to the classical equations of motion.

For any observable O , which is a function of the field, one has, for fixed time τ ,

$$\langle O(\phi(\tau)) \rangle = \int D\eta P(\eta) O(\phi(\tau)),$$

from which it follows straightforwardly using the Langevin equation and $\langle \eta \rangle = 0$, one has

$$\frac{d}{d\tau} \langle O(\phi(\tau)) \rangle = \left\langle \frac{\delta O}{\delta \phi(\tau, x)} \partial_\tau \phi(\tau, x) \right\rangle = - \left\langle \frac{\delta O}{\delta \phi(\tau, x)} \frac{\delta S}{\delta \phi(\tau, x)} \right\rangle.$$

It follows trivially that for $O(\phi) = \phi(\tau, x)$

$$\frac{d}{d\tau} \langle \phi(\tau, x) \rangle = - \left\langle \frac{\delta S}{\delta \phi(\tau, x)} \right\rangle \xrightarrow{\text{Equilibrium}} \left\langle \frac{\delta S}{\delta \phi(\tau, x)} \right\rangle = 0.$$

This also provides a consistency check for the correct implementation of the simulation, since the drift $K_\phi = -\delta S / \delta \phi$ is computed numerically during the evolution. One can also derive a correspondent Fokker-Planck equation [65], which can be proven to have a stationary distribution if the action is bounded from below, given by [64]

$$\mathcal{P}(\phi) = \frac{1}{Z} \exp(-S[\phi]). \quad (2.9)$$

This allows one to compute correlation functions as moments of the probability distribution (2.9). In particular, one has

$$\langle O \rangle_{P(\eta)} = \langle O \rangle_{\mathcal{P}(\phi)} \equiv \langle O \rangle. \quad (2.10)$$

Hence, the introduction of a white noise in the Langevin evolution (2.6), leads to the probability distribution (2.9), which is the same factor that one gets in the standard path integral quantisation of quantum field theory.

2.3.2 Stochastic quantisation with coloured noise

In the stochastic quantisation procedure the noise which accounts for the quantum fluctuations of the theory is assumed to be white, as defined in equations (2.7), (2.8). We now want to examine the dynamics in presence of a coloured noise, writing the Langevin equation as

$$\partial_\tau \phi(x, \tau) = - \frac{\delta S[\phi]}{\delta \phi(\tau, x)} + \eta_{\text{col}}(x, \tau),$$

with $\eta_{\text{col}}(x, \tau) = r_\Lambda(x) \eta(x, \tau)$. In particular, here we restrict to the regulating function defined as a sharp cutoff in momentum space

$$r_\Lambda(p) = \theta(\Lambda^2 - p^2). \quad (2.11)$$

The noise field in momentum space is then

$$\begin{aligned} \eta_{\text{col}}(p, \tau) &= \mathcal{F}[\eta_{\text{col}}(x, \tau)] = \mathcal{F}[r_\Lambda(x, \tau) \eta(x, \tau)] = \mathcal{F}[r_\Lambda(p, \tau)] \star \mathcal{F}[\eta(p, \tau)] \\ &= \theta(\Lambda^2 - p^2) \eta(p, \tau), \end{aligned}$$

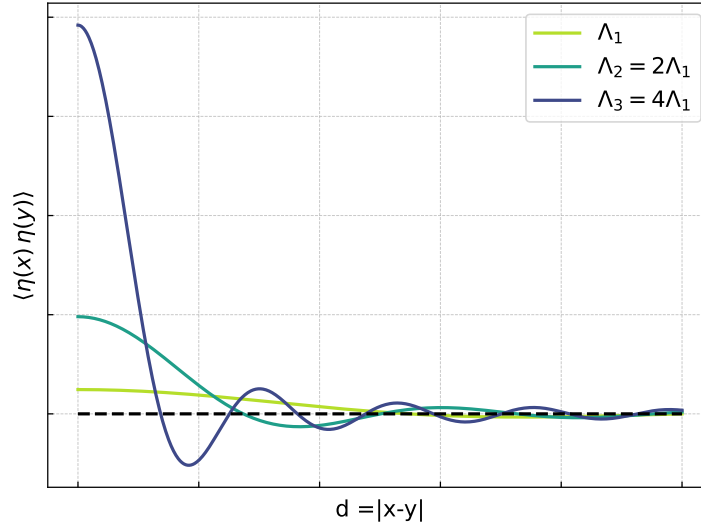


FIGURE 2.3: Noise correlation as a function of $d = |x - y|$ for three different values of the cutoff $\Lambda_1 < \Lambda_2 < \Lambda_3$, in arbitrary units. The plot is qualitative, but shows clearly that with a regulated noise, only the short-distance behaviour is affected.

where \mathcal{F} indicates the Fourier transform and \star the convolution product. An interesting quantity to look at is the position space noise correlation function

$$\begin{aligned}
 C_\eta(x, \tau, y, \tau') &= \langle \eta_{\text{col}}(x, \tau) \eta_{\text{col}}(y, \tau') \rangle \\
 &= \frac{1}{(2\pi)^4} \int D\eta P(\eta) \left[\int_{p,q} e^{-ipx - iqy} \eta_{\text{col}}(p, \tau) \eta_{\text{col}}(q, \tau') \right] \\
 &= \frac{1}{(2\pi)^4} \int_{p,q} e^{-ipx - iqy} \int D\eta [P(\eta) \eta(p, \tau) \eta(q, \tau')] \\
 &\quad \times \theta(\Lambda^2 - p^2) \theta(\Lambda^2 - q^2) \\
 &= \frac{2}{(2\pi)^2} \int_{p,q} e^{-ipx - iqy} \delta(p + q) \theta(\Lambda^2 - p^2) \theta(\Lambda^2 - q^2) \delta(\tau - \tau') \\
 &= \frac{2}{(2\pi)^2} \int_p e^{-ip(x-y)} \theta(\Lambda^2 - p^2) = \frac{1}{\pi} \int_0^\Lambda d\omega \omega J_0(\omega|x-y|),
 \end{aligned} \tag{2.12}$$

where $J_0(x)$ is a Bessel function of the first order. The integral in the last line is computed numerically as a function of $d = |x - y|$ and reported in Figure 2.3 for three different values of the cutoff $\Lambda_1 < \Lambda_2 < \Lambda_3$. This shows clearly that for $|x - y| \ll 1/\Lambda$ the noise is now correlated, while for $|x - y| \gg 1/\Lambda$ the correlation function vanishes, as in the white noise case. In other words, only the short-length behaviour of the system is affected by the introduction of such a regulating term, as one could expect.

Another intuitive and interesting aspect of the dynamics in the presence of coloured noise can be deduced by looking at the field expression in terms of the retarded Langevin Green function [64], which is here not derived, but reported from [66]

$$\phi(x, \tau) = \int_{x'} \int_{-\infty}^{\tau} d\tau' G(x - x', \tau - \tau') \left[r_\Lambda(\Delta_x) \eta(x, \tau') - \frac{\delta S}{\delta \phi} \Big|_{p=0} \phi(x', \tau) \right],$$

where

$$G(x - x', \tau - \tau') = \theta(\tau - \tau') \int_p e^{-ip \cdot (x - x')} e^{-(\tau - \tau')(p^2 + m^2)}.$$

By looking at the first term in the square bracket, one can conclude that there is no propagation of modes with momentum $p^2 \geq \Lambda^2$ due to the noise term, but one can still have contribution from modes $p^2 > \Lambda^2$ from the second term, which corresponds to the deterministic part of the equations of motion. Stated differently, UV quantum fluctuations with $p^2 > \Lambda^2$ are removed from the dynamics of ϕ , but classical degrees of freedom still contribute.

Generally speaking, the stationary distribution probability of the regulated stochastic process is given by [66]

$$\mathcal{P}_\Lambda(\phi) = \frac{1}{Z} \exp(-S_\Lambda[\phi]) = \frac{1}{Z} \exp(-(S[\phi] + \Delta S_\Lambda[\phi])), \quad (2.13)$$

where the correction term $\Delta S_\Lambda[\phi]$ reads, for a regulator $r_\Lambda(p^2)$,

$$\Delta S_\Lambda[\phi] = \frac{1}{2} \int_p \phi(p) \Lambda^2 \left(\frac{1}{r_\Lambda(p^2)} - 1 \right) \phi(-p).$$

Note that this is precisely the same regulating term that implements the cutoff on the action in the context of the Wilsonian RG, as it was shown in equation (2.2). This observation opens a deep connection between stochastic quantisation with coloured noise and the (functional) renormalisation group.

2.4 Chiral symmetry

In this section we want to introduce chiral symmetry and its breaking, both in the continuum and on the lattice.

It is useful to adopt the notation

$$\psi = (\psi^{(1)}, \dots, \psi^{(N_f)}).$$

We then introduce left-handed and right-handed spinors

$$\psi_L = (1 - \gamma_5) \psi, \quad \psi_R = (1 + \gamma_5) \psi,$$

for which

$$\psi = \frac{(1 - \gamma_5)}{2} \psi + \frac{(1 + \gamma_5)}{2} \psi = \psi_L + \psi_R.$$

2.4.1 Chiral symmetry in the continuum

The free massless Dirac Lagrangian

$$\mathcal{L}_D = \bar{\psi} \not{\partial} \psi = \bar{\psi}_L \not{\partial} \psi_L + \bar{\psi}_R \not{\partial} \psi_R \quad (2.14)$$

is symmetric under the chiral group $SU(N_f)_L \times SU(N_f)_R$, namely

$$\begin{aligned} \psi_L(x) &\rightarrow U_L \psi_L(x), & \bar{\psi}_L(x) &\rightarrow \bar{\psi}_L(x) U_L^\dagger, \\ \psi_R(x) &\rightarrow U_R \psi_R(x), & \bar{\psi}_R(x) &\rightarrow \bar{\psi}_R(x) U_R^\dagger, \end{aligned}$$

for $U_L, U_R \in SU(N_f)$.

In terms of the full spinor ψ , the chiral symmetry can be written as

$$\psi \rightarrow M \psi, \quad \bar{\psi} \rightarrow \bar{\psi} M^\dagger,$$

where

$$M = e^{i(\theta_a \tau^a + \gamma_5 \beta_a \tau^a)}$$

and $\tau^a \in su(N_f)$ are the generators of the Lie algebra of $SU(N_f)$, and for the particular case of $N_f = 2$ they are the Pauli matrices.

One can then see the chiral group as

$$SU(N_f)_L \times SU(N_f)_R \simeq SU(N_f)_V \times SU(N_f)_A,$$

where $SU(N_f)_V$ is the isospin subgroup, characterised by $\beta_a = 0$, and $SU(N_f)_A$ is the axial rotation subgroup, characterised by $\theta_a = 0$.

To be more precise, the full invariance group of the classical action is

$$SU(N_f)_L \times SU(N_f)_R \times U(1)_A \times U(1)_V,$$

where the axial and vector symmetry transformations are, respectively,

$$\psi \rightarrow e^{i\theta\gamma_5} \psi, \quad \psi \rightarrow e^{i\theta} \psi.$$

One can thus prove that axial symmetry is broken by quantum anomalies (see for example [67]), so that the symmetry in the quantum case is

$$SU(N_f)_L \times SU(N_f)_R \times U(1)_V.$$

If equal masses for each flavour are introduced, the classical action assumes the form

$$\mathcal{L}_D = \bar{\psi} \not{\partial} \psi = \bar{\psi}_L \not{\partial} \psi_L + \bar{\psi}_R \not{\partial} \psi_R + m (\bar{\psi}_R \psi_L + \bar{\psi}_L \psi_R) \quad (2.15)$$

and one can see that the mass term breaks the symmetry explicitly. This motivates the introduction of the chiral condensate

$$\langle \bar{\psi} \psi \rangle = \bar{\psi}_R \psi_L + \bar{\psi}_L \psi_R$$

as an order parameter for chiral symmetry. In the presence of equal masses, the symmetry group reduces to the isospin subgroup, diagonal in flavour space

$$SU(N_f)_V \times U(1)_V.$$

Finally, if the fermions have different masses, the symmetry group reduces to

$$\underbrace{U(1) \times \cdots \times U(1)}_{N_f} \times U(1)_V.$$

2.4.2 Chiral symmetry on the lattice

The essence of chiral symmetry for fermions can be expressed as [21]

$$\{\gamma_5, D\} = 0. \quad (2.16)$$

Implementing chiral symmetry on a finite-volume spacetime lattice is a hard task. This is because, as proven by Nielsen and Ninomiya [68], one either has chiral symmetry, or solves the doubling problem. In particular, the insertion of the Wilson term in the action, as shown in Appendix B, causes explicit breaking of the symmetry. This fact makes Wilson fermions not the most appealing choice to study chiral properties on the lattice. Thus, many options have been proposed to circumvent the issue. As an example we mention the approach by Ginsparg and Wilson [69], who proposed to modify the chiral symmetry condition (2.16) to

$$\{\gamma_5, D\} = a D \gamma_5 D$$

The right hand-side of the equation vanishes in the continuum limit $a \rightarrow 0$. In this way, one can define chiral symmetry on the lattice remaining consistent in the continuum. This approach will not be pursued further and we ask the reader to consult appropriate references [20, 21] for a detailed treatment. Our approach to study chiral symmetry will be discussed and motivated in Section 5.2.

2.5 Yukawa theory

2.5.1 Description of the model

Let us consider the Yukawa theory defined by the action

$$\begin{aligned} S[\phi, \psi, \bar{\psi}] &= S_\phi[\phi] + S_\psi[\psi, \bar{\psi}] + S_{\text{int}}[\phi, \psi, \bar{\psi}], \\ S_\phi[\phi] &= \int_x \phi_x \left(-\frac{\partial_x^2}{2} + \frac{m_\phi^2}{2} \right) \phi_x + \frac{\lambda}{4!} \phi_x^4, \\ S_\psi[\psi, \bar{\psi}] &= \int_x \sum_{f=1}^{N_f} \bar{\psi}_x^{(f)} (\not{\partial}_x + m_q) \psi_x^{(f)}, \\ S_{\text{int}}[\phi, \psi, \bar{\psi}] &= \int_x \sum_{f=1}^{N_f} g \bar{\psi}_x^{(f)} \phi_x \psi_x^{(f)}. \end{aligned} \quad (2.17)$$

One can see that the action is made of a scalar part $S_\phi[\phi]$, a fermionic part $S_\psi[\psi, \bar{\psi}]$ and a Yukawa interaction term $S_{\text{int}}[\phi, \psi, \bar{\psi}]$.

In practice we will work with fixed number of flavours $N_f = 2$, but it is useful to keep track of N_f and set it to its value when needed.

It is also convenient for later purposes to define the operators K, D represented in position space as

$$\begin{aligned} K(x, y) &= \left(-\partial_x^2 + m_\phi^2 \right) \delta(x, y), \\ D(x, y) &= (\not{\partial}_x + m_q + g\phi) \delta(x, y), \end{aligned} \quad (2.18)$$

and in momentum space as

$$\begin{aligned}\tilde{K}(p, q) &= \int_{x, y} e^{-ipx} \left(\partial_x^2 + m_\phi^2 \right) \delta(x, y) e^{iqy} = \left(\frac{p^2}{2} + \frac{m_\phi^2}{2} \right) \delta(p, q), \\ \tilde{D}(p, q) &= \int_{x, y} e^{-ipx} (\not{\partial}_x + m_q + g\phi) \delta(x, y) e^{iqy} = (\not{p}_x + m_q + g\phi) \delta(p, q).\end{aligned}\tag{2.19}$$

This allows one to rewrite the action as

$$S[\phi, \psi, \bar{\psi}] = \int_{x, y} \left[\frac{1}{2} \phi_x K_{xy} \phi_y + \frac{\lambda}{4!} \phi_x^4 \delta(x, y) + \sum_{f=1}^{N_f} \bar{\psi}_x^{(f)} D_{xy} \psi_y^{(f)} \right].$$

2.5.2 Chiral symmetry in the Yukawa model

The action written in terms of ψ_L, ψ_R , reads

$$S = S_\phi + \int_x [\bar{\psi}_L D \psi_L + \bar{\psi}_R D \psi_R + (m_q + g\phi) (\bar{\psi}_L \psi_R + \bar{\psi}_R \psi_L)]. \tag{2.20}$$

The action is not invariant under the full chiral group, but if $m_q = 0$ it is symmetric under the discrete chiral transformation

$$\begin{aligned}\phi &\rightarrow -\phi, \\ \psi_L &\rightarrow \gamma_5 \psi_L, & \bar{\psi}_L &\rightarrow -\bar{\psi}_L \gamma_5, \\ \psi_R &\rightarrow \gamma_5 \psi_R, & \bar{\psi}_R &\rightarrow -\bar{\psi}_R \gamma_5.\end{aligned}$$

This symmetry can be found in other toy models for QCD such as the Gross-Neveu model [42]. In order to generalise the model to the full chiral group, one has to consider an $O(4)$ scalar sector and interactions, since $O(4) \simeq SU(2) \times SU(2)$. Similar effective theories for QCD with such properties are, for example, the Nambu – Jona-Lasinio model [40, 41] and the Quark-Meson model [43–45]. Thus, since this work is based on $1 + 1$ spacetime dimensions, spontaneous breaking of continuous symmetries is forbidden by the Mermin-Wagner theorem [70], hence we decided to opt for the $O(1)$ version.

We now want to discuss more in detail the phenomenom of (discrete) chiral symmetry breaking and how it can happen in the model. In fact, the latter can happen either explicitly in the classical action, if a finite quark mass is added, or spontaneously, if $\langle \phi \rangle \neq 0$.

To better see this, let us perform the fermionic path integral explicitly

$$\int \mathcal{D}\psi \mathcal{D}\bar{\psi} \exp \left(- \int_x \sum_{f=1}^{N_f} \bar{\psi}_x^{(f)} D \psi_x^{(f)} \right) = (\det D[\phi])^{N_f} = e^{N_f \text{Tr} \log(D[\phi])},$$

where the trace is performed over spacetime and spinor components.

The full path integral can now be expressed in terms of the resulting effective action for the scalar fields

$$Z = \int \mathcal{D}\phi e^{-S_{\text{eff}}[\phi]},$$

with

$$S_{\text{eff}}[\phi] = S_\phi[\phi] - N_f \text{Tr}_{x,s} \log D[\phi]. \tag{2.21}$$

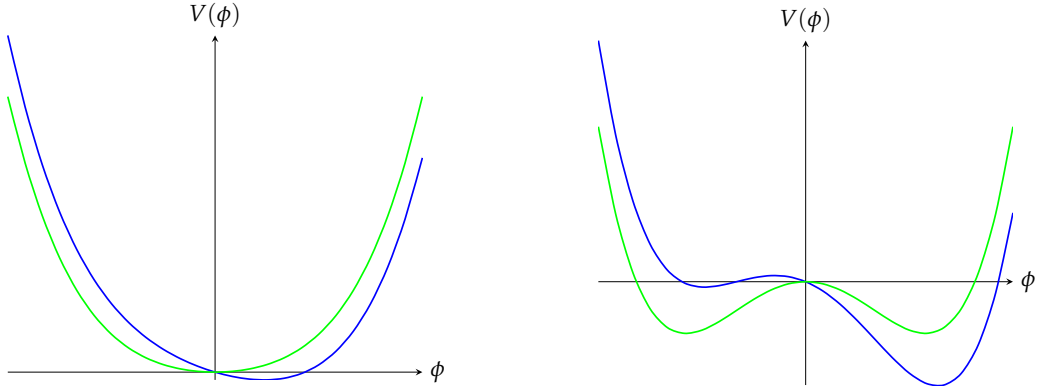


FIGURE 2.4: Symmetry breaking in the Yukawa model.
 (Left) Classical potential for $m_\phi^2 < 0$. (Right) Classical potential for $m_\phi^2 > 0$.

One can derive the classical equations of motion by imposing $\frac{\delta S}{\delta \phi} = 0$, here expressed in momentum space

$$(k^2 + m_\phi^2) \phi(x) + \frac{\lambda}{6} \phi^3(x) = N_f g \text{Tr}_s [D^{-1}(\phi(x))] = -N_f g \bar{\psi}(x) \psi(x). \quad (2.22)$$

For $\lambda = 0$, they highlight a simple proportionality relation between magnetisation and chiral condensate, which reads

$$\phi = -\frac{N_f g}{k^2 + m_\phi^2} \bar{\psi} \psi. \quad (2.23)$$

This relation, which was here derived at the classical level, is proven to hold also in mean field on the quantum level [71] and makes apparent the role of ϕ as a quark bilinear. When bosons self-interactions are added, namely when $\lambda \neq 0$, the full relation between ϕ and the chiral condensate $\bar{\psi} \psi$ is given by (2.23), but still one expects, qualitatively,

$$\langle \phi \rangle \sim \langle \bar{\psi} \psi \rangle. \quad (2.24)$$

A non-vanishing condensate is also related to a physical quark mass [71, 72], while the presence of magnetisation causes the breaking of $O(1)$ symmetry. If $\langle \phi \rangle = v$, one can write $\phi(x) = v + \varphi(x)$ and the massless lagrangian assumes the form

$$S = S_\phi + \int_x [\bar{\psi}_L D \psi_L + \bar{\psi}_R D \psi_R + g v (\bar{\psi}_L \psi_R + \bar{\psi}_R \psi_L)] + g \varphi(x) (\bar{\psi}_L \psi_R + \bar{\psi}_R \psi_L), \quad (2.25)$$

hence showing that one can expect

$$\langle \phi \rangle \sim \langle \bar{\psi} \psi \rangle \sim m_q. \quad (2.26)$$

Figure 2.4 depicts the classical potential in the Yukawa theory. The $O(1)$ symmetry of the scalar sector is manifested in a single minimum located at $\phi = 0$ if $m_\phi^2 > 0$, or in two equivalent minima if $m_\phi^2 < 0$. As the Yukawa interaction is introduced, the symmetry can be broken either explicitly in presence of a fermionic bare mass, or spontaneously if the scalar field gains a non-zero expectation value. In this case, the classical potential assumes the shape given by the green line.

Chapter 3

Methods and algorithms

3.1 Discretisation of the Yukawa theory

In order to make the theory suitable for a numerical simulation on a computer, the continuum formulation of the Yukawa model, which has been introduced in Section 2.5, has to be discretised. Here we provided a sketch of a discretisation procedure, and we refer to other resources [19–22] for further details.

For what concerns the bosonic part of the action, a discretisation can be done straightforwardly with the following replacements

$$\begin{aligned} \int d^x &\rightarrow a^2 \sum_x, \\ \partial_t^2 + \partial_x^2 &= \frac{\partial^2}{\partial t^2} + \frac{\partial^2}{\partial x_1^2} \rightarrow \sum_\mu \left[\frac{\delta_{m,n+\mu} + \delta_{m,n-\mu} - 2\delta_{m,n}}{a^2} \right], \end{aligned}$$

which yields to the lattice action

$$\begin{aligned} S_\phi[\phi] &= a^2 \left(\frac{1}{2} \sum_{m,n} \phi_m K_{mn} \phi_n + \frac{\lambda}{4!} \sum_n \phi_n^4 \right) \\ &= \frac{1}{2} \sum_{m,n} \hat{\phi}_m \hat{K}_{mn} \hat{\phi}_n + \frac{\hat{\lambda}}{4!} \sum_n \hat{\phi}_n^4, \end{aligned}$$

where we expressed everything in dimensionless quantities

$$\begin{aligned} \hat{m}_\phi^2 &= a^2 m_\phi^2, \\ \hat{\lambda} &= a^2 \lambda, \\ \hat{K}_{mn} &= a^2 K_{mn}. \end{aligned} \tag{3.1}$$

The operator components \hat{K}_{mn} are the discretised version of (2.18)

$$\hat{K}_{mn} = - \sum_\mu [\delta_{m,n+\mu} + \delta_{m,n-\mu} - 2\delta_{m,n}] + \hat{m}_\phi^2 \delta_{mn}, \tag{3.2}$$

and its representation in momentum space is

$$\begin{aligned}
\hat{K}_{p,q} &= \sum_{n,m} e^{ipn} \hat{K}_{nm} e^{-iqm} \\
&= \sum_{n,m} e^{ipn} \left(- \sum_{\mu} [\delta_{m,m+\hat{\mu}} + \delta_{m,m-\hat{\mu}} - 2\delta_{m,n}] + \hat{m}_{\phi}^2 \delta_{mn} \right) e^{-iqm} \\
&= \sum_n e^{i(p-q)n} \left[\hat{m}_{\phi}^2 + 2 \sum_{\mu} (1 - \cos(q_{\mu})) \right] \\
&= \left[\hat{m}_{\phi}^2 + \sum_{\mu} 4 \sin^2 \left(\frac{p_{\mu}}{2} \right) \right] \delta(p-q).
\end{aligned}$$

For what concerns the fermionic action, a naïve discretisation is not sufficient, due to the well known doubling problem [19, 20]. In this work Wilson fermions [23] are employed as a way to fix such issue. Details of this formulation are explained in Appendix B. Here, only the final discretised action is reported, which reads

$$S_{\psi} [\hat{\psi}, \bar{\psi}] + S_{\text{int}} [\hat{\phi}, \hat{\psi}, \bar{\psi}] = \sum_{f=1}^{N_f} \bar{\psi}_m^{(f)} \hat{D}_{mn} \hat{\psi}_n^{(f)}, \quad (3.3)$$

with $\psi_n^{(f)}$ being a two-component spinor, and $\hat{D}_{m,n}$ the Wilson-Dirac operator defined as

$$\begin{aligned}
\hat{D}_{m,n} &= - \left(\frac{\Gamma_{+\hat{0}}}{2} \delta_{m,m+\hat{0}} + \frac{\Gamma_{-\hat{0}}}{2} \delta_{m,m-\hat{0}} + \frac{\Gamma_{+\hat{1}}}{2} \delta_{m,m+\hat{1}} + \frac{\Gamma_{-\hat{1}}}{2} \delta_{m,m-\hat{1}} \right) \\
&\quad + (2ar + \hat{m} + \hat{g}\phi) \delta_{s,s'} \delta_{m,n}.
\end{aligned} \quad (3.4)$$

Note that the interaction term $g \bar{\psi}\phi\psi$ has been included in the definition of D . The Wilson projectors $\Gamma_{\pm\hat{\mu}}$ are defined as

$$\Gamma_{\pm\hat{\mu}} = ar \mathbb{1}_s \mp \gamma_{\mu}.$$

Since $r \in [0, 1]$ is a free parameter, in this work we set $r = 1$, if not otherwise specified.

In summary the discretised action for the Yukawa model is

$$S [\hat{\phi}, \hat{\psi}, \bar{\psi}] = \sum_{m,n} \hat{\phi}_m \hat{K}_{m,n} \hat{\phi}_n + \frac{\hat{\lambda}}{4!} \hat{\phi}_m^4 \delta_{m,n} + \sum_{f=1}^{N_f} \bar{\psi}_m^{(f)} \hat{D}_{mn} \hat{\psi}_n^{(f)}, \quad (3.5)$$

with $\hat{K}_{mn}, \hat{D}_{mn}$ given respectively by (3.2) and (3.4).

For later reference, we also report the discretised version of the effective action (2.21)

$$\begin{aligned}
S_{\text{eff}}[\hat{\phi}] &= S_{\phi}[\hat{\phi}] - N_f \text{Tr}_{n,s} \log \hat{D} \\
&= \sum_{m,n} \hat{\phi}_m \hat{K}_{m,n} \hat{\phi}_n + \frac{\hat{\lambda}}{4!} \hat{\phi}_m^4 \delta_{m,n} - N_f \text{Tr}_{n,s} \log \hat{D}_{nn}.
\end{aligned} \quad (3.6)$$

The full discrete path-integral reads

$$Z = \int \prod_n d\hat{\phi}_n e^{-S_{\text{eff}}[\hat{\phi}]}. \quad (3.7)$$

In the remainder of this work, both the original action S and the effective action S_{eff} will be denoted by S for simplicity. It will be clear from the context which of the two we will be referring to.

3.2 Langevin Monte Carlo

The relations (2.9) and (2.10) suggest that equation (2.6) can be integrated numerically for discrete time steps τ_n to generate field configurations distributed according to (2.9). The simplest first-order integration algorithm is the Euler-Maruyama scheme [63]

$$\phi(\tau_{n+1}, x) = \phi(\tau_n, x) - \epsilon \frac{\delta S[\phi]}{\delta \phi(\tau_n, x)} + \sqrt{\epsilon} \eta(\tau_n, x) + O(\epsilon^2),$$

where $\epsilon = \tau_{n+1} - \tau_n$. Higher order integration schemes are possible (see e.g. [73, 74]), but not adopted in this work, and an adaptive step size is employed. In this way, for any observable O , one can introduce a Monte-Carlo estimator $\langle O \rangle_*$ which converges to the expectation value given by (2.10) in the limit of infinite samples

$$\langle O \rangle_* = \frac{1}{N_{\text{samp}}} \sum_{i=1}^{N_{\text{samp}}} O_i \xrightarrow{N_{\text{samp}} \rightarrow \infty} \langle O \rangle = \frac{1}{Z} \int D\phi O(\phi) \exp(-S[\phi]), \quad (3.8)$$

where $O_i = O(\phi(\tau_i))$ is the sample of the observable O done at time τ_i .

For the discretised action of the Yukawa theory (3.6) the drift reads, explicitly,

$$\begin{aligned} \frac{\partial S}{\partial \hat{\phi}_m(\tau_n)} &= \frac{\partial S_{\hat{\phi}}}{\partial \hat{\phi}_m(\tau_n)} - N_f \text{Tr}_s \left[\sum_{j,k} \hat{D}_{jk}^{-1} \frac{\partial \hat{D}_{kj}(\hat{\phi})}{\partial \hat{\phi}_m(\tau_n)} \right] \\ &= \sum_l \hat{K}_{ml} \hat{\phi}_l + \frac{\hat{\lambda}}{6} \hat{\phi}_m^3 - \hat{g} N_f \text{Tr}_s \left[(\hat{D}_{mm})^{-1}(\hat{\phi}(\tau_n)) \right]. \end{aligned} \quad (3.9)$$

While the bosonic contribution can be computed in a straightforward manner, the computation of the fermionic contribution requires the inversion of the Dirac operator. This, in general, cannot be done straightforwardly, mainly due to computational reasons. The full Dirac operator would be a $(2 \cdot N_t \cdot N_x \cdot N_f)^2$ dimensional object and a full inversion would be very expensive. In fact, D^{-1} has to be recomputed at every step and the best available algorithm as today for the matrix inversion has a computational complexity of $O(n^{2.371552})$ [75]. To circumvent this, we use the bilinear noise scheme [73, 76] in combination with the Conjugate Gradient algorithm to evaluate the trace, as detailed in Appendix C, avoiding to invert the full matrix.

3.3 Applications of coloured noise in lattice QFT

After the general introduction on coloured noise given in Section 2.3.2, let us now look more closely on the lattice formulation and at some possible applications of the technique, some of which will be studied numerically in Chapter 5.

To this end, let us consider a two-dimensional lattice with side lengths L_t, L_x and spacing $a = a_x = a_t$. This implies a maximum momentum $p_{\max} = \pi/a$ in each spacetime direction and $N_x = L_x/a, N_t = L_t/a$ points in each direction. Let us also define

$$\Lambda_0^2 \equiv (p_{\max}^x)^2 + (p_{\max}^t)^2, \quad (3.10)$$

which indicates the maximum squared momentum on the given lattice.

We then consider a simulation with a regularised noise defined by a cutoff $\Lambda \leq \Lambda_0$ and we define a dimensionless parameter

$$s^2 = \frac{\Lambda^2}{\Lambda_0^2}, \quad 0 \leq s \leq 1. \quad (3.11)$$

Note that Λ implicitly defines a length scale given by $a_{\text{eff}} = \pi/\Lambda$.

3.3.1 Classical-to-quantum interpolation

The use of coloured noise allows for a smooth interpolation between the fully classical and fully quantum pictures. In fact, one can perform various simulations changing the value of the cutoff fraction s and adding or removing quantum degrees of freedom. This can be used either to investigate the role of quantum fluctuations in the system or to remove irrelevant degrees of freedom, resulting in a speed-up of the simulation.

3.3.2 Noise-induced transition

Noise-induced transition is a well-known field of stochastic dynamics [65, 77] and consists in investigating whether noise can qualitatively affect the behaviour of a system. In our case, since noise is due to quantum fluctuations, we are interested in understanding if quantum fluctuations can trigger a phase transition with respect to the classical system, with the same parameter settings.

This question will be addressed in Section 5.2 and it will be shown that for small negative bosonic mass squared, the classical system lies in a state of broken symmetry, while in the quantum case, the symmetry is restored.

Note that there is a subtle distinction between noise-induced transitions and noise-induced phase transitions [78]. In simple words, the former refer to the possibility for the system to change its state qualitatively due to the introduction of noise. On the other side, a noise-induced phase transition is characterised by a change in the order parameter which persists at equilibrium. Strictly speaking, in a finite volume lattice simulation, one cannot observe phase transitions, since the latter can only be reached in the infinite volume limit, with an infinite number of configurations [62]. This issue will be briefly addressed in Section 5.2.

3.3.3 Cooling and the continuum limit of effective theories

Following the paradigm of Kadanoff-Wilson of Chapter 2, we want to use RG properties to encode quantum fluctuations in a redefinition of the couplings of the bare action. This removes short-distance fluctuations from the simulation, without changing the physical content of the theory in terms of expectation values.¹ Note that this would, in principle, require a detailed knowledge of the β -functions of the theory. Thus, for a sufficiently high cutoff, approximate Ansatz such as dimensional rescalings are generally enough. We will pursue this way, as follows:

Let us consider a simulation with $s = 1$ and a set of bare couplings $\{g_0^i\}$, and another simulation with $s' < 1$ and a new set of couplings $\{g_0^{i'}\}$.

For what concerns the scalar part of the action, a dimensional rescaling, which corresponds to a tree-level RG transformation, is rather straightforward

$$\begin{aligned} \hat{m}_\phi^2 = (a^2 m_\phi^2) &\rightarrow s^2 (a^2 m_\phi^2) = s^2 \hat{m}_\phi^2, & \hat{\lambda} = (a^2 \lambda) &\rightarrow s^2 (a^2 \lambda) = s^2 \hat{\lambda}, \\ \hat{\phi} = \phi &\rightarrow \phi = \hat{\phi}. \end{aligned}$$

The fermionic part needs some more careful analysis. For simplicity, let us for the moment set $N_f = 1$.

In a lattice simulation one wants to perform the integral over the fermionic fields and work with the effective action (2.21). In this case the drift is given by equation (3.9), with the fermionic contribution

$$K_\psi = g \text{Tr}_s D^{-1}, \quad (3.12)$$

or, in terms of dimensionless quantities,

$$\hat{K}_\psi = (ag) \text{Tr}_s (aD)^{-1}.$$

This implies that under a lattice block-spin transformation, where $a \rightarrow sa$,

$$\hat{K}_\psi \rightarrow (sag) \text{Tr}_s (saD)^{-1} = \hat{K}_\psi. \quad (3.13)$$

On the other side, when computing the drift via the original action (2.17), one gets

$$\begin{aligned} K &= -\frac{\delta S}{\delta \phi} = K_\phi - g \bar{\psi} \psi = \\ &= -K \phi - \frac{\lambda}{6} \phi^3 - g \bar{\psi} \psi, \end{aligned} \quad (3.14)$$

where, in the last row, K indicates the bosonic operator whose components are given by (3.2). The fermionic contribution is given by

$$K'_\psi = -g \bar{\psi} \psi.$$

Note that all the terms in the equation (3.14) have dimension 2, in units of energy, which means, in particular, that after a lattice block-spin transformation where $a \rightarrow sa$, one has

$$\hat{K}'_\psi = (ag)(a\bar{\psi}\psi) \rightarrow s^2(ag)(a\bar{\psi}\psi) = s^2 \hat{K}'_\psi, \quad (3.15)$$

in contrast with (3.13). For this reason, in order to have the correct scaling, we compute the contribution to the drift without rescaling the Dirac operator (and hence the

¹This fact attributes the name cooling to the procedure.

Yukawa coupling), and then rescale the whole drift via

$$\hat{K}_\psi \rightarrow s^2 \hat{K}_\psi,$$

so that the scaling dimension of the other terms in (3.14) is matched.

We want to mention that the cooling procedure has important consequences on the issue of continuum limit of low-energy effective theories. In fact, in the standard lattice regularisation procedure, one always has $a \sim \Lambda_0^{-1}$, which means that the continuum limit $a \rightarrow 0$ is always connected to the limit $\Lambda_0 \rightarrow \infty$, in accordance to what discussed in sections 2.1 and 2.2. By means of $\Lambda = s\Lambda_0$, one can keep an effective cutoff fixed at the desired scale while taking the limit $a \rightarrow 0, \Lambda_0 \rightarrow \infty$. This allows for the continuum limit of the effective theory at scale Λ , which is important to reduce lattice artifacts and to allow for a comparison with continuum methods.

3.3.4 Control over temperature

The use of coloured noise allows one to access a wider and finer range of temperatures. In fact, as already mentioned in Section 2.2, the temperature on the lattice is given by

$$T = \frac{1}{a N_t}. \quad (3.16)$$

Hence one can change temperature either by changing the spacing a or by changing the number of points in the time direction N_t . Both approaches pose serious constraints on the range of accessible temperatures. The spacing a is often determined by the energy scale at which one wants to simulate theory. For example in an effective theory, as explained in Section 2.2, one has to keep $\Lambda \leq \Lambda_{\text{phys}}$, and since $a = \pi/\Lambda$, one ends with a constraint on the spacing $a \geq \pi/\Lambda_{\text{phys}}$.

The highest temperature reachable is then limited by mathematical arguments as one cannot have $N_t < 1$, even though in a simulation one often needs $N_t \geq 2$. On the other side, the minimum temperature reachable is limited by computational resources as one cannot afford $N_t \rightarrow \infty$. Moreover, the resolution of high temperatures is very coarse due to the relation (3.16), in the sense that for small N_t , a change in the number of time points causes a significant variation in the temperature.

By means of coloured noise, one can change the temperature by changing the effective spacing. In fact, if one follows the cooling procedure by keeping N_t fixed, one sets a new temperature which is given by

$$T_{\text{eff}} = \frac{1}{a_{\text{eff}} N_t} = \frac{1}{sa N_t} = T/s,$$

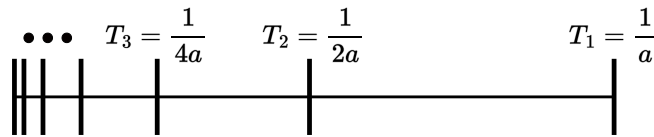


FIGURE 3.1: Pictorial representation of the accessible temperatures in a standard lattice simulation. Since $T = 1/aN_t$, there is a low resolution of temperatures for small N_t , and a bounded range of values that can be accessed for fixed a .

where $s = \Lambda_{\text{eff}}/\Lambda \leq 1$. Note that not only the temperature has been raised, but one has also gained resolution around T_{eff} . In fact, to reach this temperature by changing N_t , one should change the number of time points to $N_t \rightarrow sN_t$, and for what explained before, a lower N_t comes with a loss of resolution.

The control over temperature will not be investigated in this work. For a more detailed explanation of the procedure and its relevance in the context of the Quark-Meson model, we refer to [79].

3.4 Definition of relevant observables

From now on, we will indicate both the dimensionless quantities and dimensionful ones by using the notation of the latter. When dealing with the discretised theory, we will be implicitly referring to the dimensionless quantities. A distinction will still be made when relevant. Moreover, a general spacetime vector will be denoted as

$$x = (t, \vec{x}),$$

where t is the temporal component and \vec{x} is the spatial component.

We define the magnetisation M of the field ϕ as

$$M = \left\langle \frac{1}{V} \sum_n \phi_n \right\rangle.$$

In a finite volume lattice system, the absolute magnetisation

$$M = \left\langle \frac{1}{V} \left| \sum_n \phi_n \right| \right\rangle$$

is better suited [21, 62] as an order parameter. In the continuum, phase transition is characterised by a divergence in the susceptibility or connected two-point function

$$\chi_2 = V \left(\langle M^2 \rangle - \langle M \rangle^2 \right) = V \langle (M - \langle M \rangle)^2 \rangle.$$

In a finite volume lattice simulation, one observes a peak that becomes sharper as the volume is increased.

In practice, the susceptibility of the order parameter

$$\chi_2 = V \langle (M - \langle |M| \rangle)^2 \rangle \quad (3.17)$$

will be adopted.

The susceptibility measures the Gaussian fluctuations of the order parameter, the magnetisation. We then introduce the Binder cumulant [80], which quantifies the curtosus of the fluctuations

$$U_L \equiv 1 - \frac{1}{3} \frac{\langle M^4 \rangle}{\langle M^2 \rangle^2}.$$

It is particular useful to characterise phase transitions in terms of the order parameter ϕ , since it assumes the values

$$U_L = \begin{cases} 0 & \text{symmetric phase,} \\ 2/3 & \text{broken phase.} \end{cases}$$

We define the fermionic two-point function

$$\begin{aligned} \langle \psi(x) \bar{\psi}(y) \rangle &= \frac{1}{Z} \int \mathcal{D}\phi \mathcal{D}\psi \mathcal{D}\bar{\psi} \psi(x) \bar{\psi}(y) \exp(-S_\phi - \psi D\psi + \bar{\eta}\psi + \bar{\psi}\eta) \\ &= \frac{1}{Z} \int \mathcal{D}\phi \mathcal{D}\psi \mathcal{D}\bar{\psi} \frac{\delta}{\delta \bar{\eta}(x)} \frac{\delta}{\delta \eta(y)} \exp(-S_\phi - \psi D\psi + \bar{\eta}\psi + \bar{\psi}\eta) \\ &= \frac{1}{Z} \int \mathcal{D}\phi \det[D(\phi)] \exp(-S_\phi) \frac{\delta}{\delta \bar{\eta}(x)} \frac{\delta}{\delta \eta(y)} \exp(\bar{\eta} D^{-1} \eta) \\ &= \left\langle [D^{-1}(\phi)]_{mn} \right\rangle, \end{aligned} \quad (3.18)$$

and its connected counterpart

$$\langle \psi(x) \bar{\psi}(y) \rangle_c = \langle \psi(x) \bar{\psi}(y) \rangle - \langle \psi(x) \rangle \langle \bar{\psi}(y) \rangle.$$

The chiral condensate can then be computed as

$$\langle \bar{\psi}\psi \rangle = \sum_{n,s} \langle \bar{\psi}_{n,s} \psi_{n,s} \rangle = -\text{Tr}_{n,s} (D^{-1})_{nn}.$$

On a finite volume lattice, the correlation of a field at two spacetime points is quantified by the correlator

$$C_\psi(t, 0) \equiv \frac{1}{V} \sum_x [\langle \psi(t, \vec{x}) \bar{\psi}(0, 0) \rangle_c - \langle \psi(N_t - t, \vec{x}) \bar{\psi}(0, 0) \rangle_c]. \quad (3.19)$$

Note that we sum up two waves because of the boundary conditions.

In momentum space, by using a spectral decomposition, one has

$$\begin{aligned} \frac{1}{V} \sum_{\vec{x}} e^{-i\vec{p}\vec{x}} \langle \bar{\psi}(t, \vec{x}) \psi(0, \vec{0}) \rangle &= \frac{1}{V} \sum_{\vec{x}} e^{-i\vec{p}\vec{x}} \sum_k \langle 0 | \bar{\psi}(t, \vec{x}) | k \rangle \langle k | \psi(0, \vec{0}) | 0 \rangle \\ &= \frac{1}{V} \sum_{\vec{x}} e^{i\vec{p}\vec{x}} \sum_k \left\langle 0 \left| e^{-ip'x} \bar{\psi}(0, \vec{0}) e^{ip'x} \right| k \right\rangle \langle k | \psi(0, \vec{0}) | 0 \rangle \\ &= \frac{1}{V} \sum_{\vec{x}} e^{-i\vec{p}\vec{x}} \sum_k e^{ikx} \langle 0 | \bar{\psi}(0, \vec{0}) | k \rangle \langle k | \psi(0, \vec{0}) | 0 \rangle \\ &= \frac{1}{V} \sum_{\vec{x}, k} e^{-i(\vec{p}-\vec{k})\vec{x}} e^{-E_k t} |\langle 0 | \psi(0, \vec{0}) | k \rangle|^2 \\ &= \frac{1}{V} \sum_k \delta(\vec{p} - \vec{k}) e^{-E_k t} |\langle 0 | \psi(0, \vec{0}) | k \rangle|^2 \\ &= \frac{1}{V} \sum_n e^{-E_n(\vec{p})t} \left| \langle 0 | \psi(0, \vec{0}) | p_n \rangle \right|^2. \end{aligned}$$

Using this, equation (3.19) can be rewritten as

$$\begin{aligned} C(t, \vec{p}) &= \frac{1}{V} \sum_{\vec{x}} e^{-i\vec{p}\vec{x}} \left(\langle \psi(t, \vec{x}) \bar{\psi}(0, \vec{0}) \rangle_c - \langle \psi(N_t - t, \vec{x}) \bar{\psi}(0, \vec{0}) \rangle_c \right) \\ &\propto \sum_n e^{-E_n(\vec{p})t} - e^{-E_n(\vec{p})(N_t - t)} = \sum_n 2e^{-E_n(\vec{p})\frac{N_t}{2}} \sinh \left[E_n(\vec{p}) \left(\frac{N_t}{2} - t \right) \right]. \end{aligned}$$

By projecting onto $p = 0$, one can note that for large times all the contributions but the ground state are suppressed, so that the fermionic correlator assumes the form

$$C_\psi(t, 0) \approx \sinh \left(E_0^\psi \left(\frac{N_t}{2} - t \right) \right), \quad (3.20)$$

where E_0^ψ is the fermionic mass gap, which will be denoted as $m_{q,\text{phys}}$.

An important quantity to compute the correlator on the lattice are the so called time slices

$$S(t, \vec{p}) = \frac{1}{V} \sum_{\vec{x}} e^{i\vec{p}\vec{x}} \psi(t, \vec{x}), \quad \bar{S}(t, \vec{p}) = \frac{1}{V} \sum_{\vec{x}} e^{i\vec{p}\vec{x}} \bar{\psi}(t, \vec{x}).$$

In fact, they are related to the correlator via

$$\begin{aligned} \langle \bar{S}(t_1, \vec{p}) S(t_2, -\vec{p}) \rangle_c &= \frac{1}{V^2} \sum_{\vec{x}} e^{-i\vec{p}\vec{x}} \sum_{\vec{y}} e^{i\vec{p}\vec{y}} \langle \bar{\psi}(t_1, \vec{x}) \psi(t_2, \vec{y}) \rangle_c \\ &= \frac{1}{V^2} \sum_{\vec{x}, \vec{y}} e^{-i\vec{p}(\vec{x} - \vec{y})} \langle \bar{\psi}(t_1, \vec{x}) \psi(t_2, \vec{y}) \rangle_c \\ &= \frac{1}{V} \sum_{\vec{r}} e^{-i\vec{p}\vec{r}} \langle \bar{\psi}(t_1, \vec{r}) \psi(t_2, \vec{0}) \rangle_c \\ &= C(t_1 - t_2, \vec{p}). \end{aligned}$$

Note that from the second row to the third row translation invariance has been assumed.

Using this result, together with (3.18) and (3.20), one gets to the chain of equalities

$$\begin{aligned} C_\psi(t, 0) &= \langle \bar{S}(t, 0) S(0, 0) \rangle = \frac{1}{N_x} \sum_{\vec{x}} \langle \bar{\psi}(t, \vec{x}) \psi(0, 0) \rangle \\ &= \frac{1}{N_x} \sum_{\vec{x}} [D^{-1}]((t, \vec{x}), (0, 0)) \\ &\approx \sinh \left(m_{q,\text{phys}} \left(\frac{N_t}{2} - t \right) \right). \end{aligned}$$

This allows to compute the correlator on the lattice and extract the physical quark mass via a fitting procedure. Note that we do not need the full inversion of the Dirac operator. One can in fact write

$$(D^{-1})_{n,0} = D_{nm}^{-1} \eta_m,$$

where

$$\eta_m = s \delta_{m,0}$$

is a spinor field, where only the component at the origin is non-zero, and is given by the spinor s . Hence, one is reduced to solve the linear system of equations

$$\sum_n D_{mn}^{-1} \psi_m = \eta_n ,$$

which can be done by means of the Conjugate Gradient algorithm, as detailed in Appendix C.

By similar arguments one can introduce the bosonic two-point function and connected two-point function

$$\begin{aligned} \langle \phi(x) \phi(y) \rangle &= \frac{1}{Z} \int \mathcal{D}\phi \mathcal{D}\psi \mathcal{D}\bar{\psi} \phi(x) \phi(y) e^{-S[\phi, \psi, \bar{\psi}]}, \\ \langle \phi(x) \phi(y) \rangle_c &= \langle \phi(x) \phi(y) \rangle - \langle \phi(x) \rangle \langle \phi(y) \rangle, \end{aligned}$$

and arrives at the bosonic correlator

$$\begin{aligned} C_\phi(t, 0) &\approx \cosh \left(E_0^\phi \left(\frac{N_t}{2} - t \right) \right) \\ &= \langle S(t, 0) S(0, 0) \rangle = \frac{1}{N_x} \sum_n \langle \phi(t, n) \phi(t, 0) \rangle_c, \end{aligned} \quad (3.21)$$

where the bosonic time slice is defined as

$$S(t, \vec{p}) = \frac{1}{V} \sum_{\vec{x}} e^{i\vec{p}\vec{x}} \phi(t, \vec{x}),$$

and for zero momentum is simply the space average of the field configuration. The hyperbolic cosine in (3.21) appears in place of the hyperbolic sine since one applies periodic boundary conditions instead of anti-periodic in equation (3.19). The last quantity which will be used in the investigation is the renormalised boson mass $m_{\phi,r}$. A practical formula for the computation of such quantity on the lattice can be derived by looking at the expression of the scalar renormalised two-points function, which for small momentum assumes the form

$$G(p) = \frac{Z_R}{\sum_\mu p_\mu^2 + m_{\phi,r}^2 + O(p^4)}.$$

The last expression evaluated at zero momentum gives the susceptibility

$$\chi_2 = G(0) = \frac{Z_R}{m_R^2}.$$

Finally, the second moment is, by definition,

$$\mu_2 = - \left. \frac{\partial^2}{\partial p_v \partial p_v} G(p) \right|_{p=0} = 2d \frac{Z_R}{m_R^4}.$$

Putting all together we arrive at

$$m_{\phi,r}^2 = 2d \frac{\chi_2}{\mu_2}.$$

This provides a way to compute the renormalised mass, since the susceptibility can be calculated via (3.17), and the second moment as

$$\mu_2 = \sum_x x^2 \langle \phi(x) \phi(0,0) \rangle_c = d N_x \langle S(t,0) S(0,0) \rangle .$$

For a more detailed derivation of these identities we refer to [66].

An important note is that translation invariance was assumed in the derivation. This does not strictly holds for every configuration, but it is assumed to hold on expectation values.

Chapter 4

Numerical investigation: preliminaries

4.1 Inversion of the Dirac operator

As mentioned in Section 3.2, the inversion of the Dirac operator is a computationally expensive operation. In fact, simple algorithms to invert a matrix such as Gaussian elimination have a computational complexity of $O(n^3)$ [81], while the best algorithm available nowadays has been proved to scale as $O(n^{2.371552})$ [75].

To circumvent this, since we are often only interested in applying the inverse matrix to a vector, we make use of the Conjugate Gradient algorithm, as detailed in Appendix C.

We now want to give an idea of the speed-up that one can gain by following such approach, keeping in mind that this is an operation which has to be performed at each evolution step. To do this, we construct a Dirac operator described by equation (3.4) with bare quark mass $m_q = 0.5$ and Yukawa coupling $g = 0.5$. We then add a fluctuating scalar field

$$\phi(x) = v + \eta(x),$$

where $v = 1.0$ and η is a normally distributed number with mean 0 and unity variance. We then measure the time needed to compute

$$\xi = D^{-1}\psi,$$

where ψ is a vector of random numbers uniformly distributed between -1 and 1 . We study the time dependence as a function of the vector size V by averaging over 20 measures per each value of V .

Figure 4.1 reports the results of the experiment. Assuming that our algorithm has complexity $O(V^b)$, namely that when $V \rightarrow \infty$,

$$t \approx a V^b,$$

we fit our data according to the model

$$\log t = \log a + b \log V.$$

We find

$$\log a = -3.1 \pm 0.1 \quad \text{and} \quad b = 1.02 \pm 0.02.$$

Note that for a standard Gaussian elimination procedure we would have found $b \approx 3.0$. This is of particular relevance in the case of this work, since the cooling technique via coloured noise requires doubling the number of lattice points in each direction at each block spin step; hence the volume of the lattice is increased by a

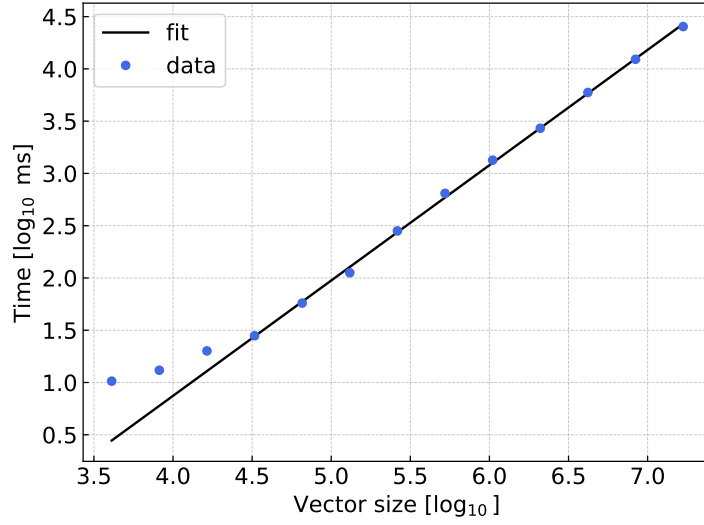


FIGURE 4.1: Computational complexity of the Conjugate Gradient algorithm in our model. The results show the operation time scales as $t \sim \mathcal{O}(V^{1.03})$ for large vector sizes, while for a standard inversion via Gaussian elimination one would have $t \sim \mathcal{O}(V^3)$.

factor 2^d at each iteration, where d is the spacetime dimension.

Typical lattices sizes in this work are up to $128 \times 128 \times N_f \times N_s \approx 10^5$, where N_f is the number of flavours and N_s is the number of spinor components. Therefore, a good volume scaling of the algorithm is strictly necessary.

4.2 The fermionic correlator

We now want to analyse the behaviour of the fermionic correlator and illustrate the fermionic masses extraction procedure.

Let us for the moment restrict to $g = 0$, so that the Dirac operator reduces to the one of free Wilson fermions

$$\begin{aligned} \hat{D}_{m,n} = & \left(\frac{\Gamma_{+\hat{0}}}{2} \delta_{m,m+\hat{0}} + \frac{\Gamma_{-\hat{0}}}{2} \delta_{m,m-\hat{0}} + \frac{\Gamma_{+\hat{1}}}{2} \delta_{m,m+\hat{1}} + \frac{\Gamma_{-\hat{1}}}{2} \delta_{m,m-\hat{1}} \right) \\ & + (2ar + \hat{m}) \delta_{s,s'} \delta_{m,n}. \end{aligned} \quad (4.1)$$

We then compute the correlator (3.20) numerically via a single inversion of the Dirac operator using the Conjugate Gradient algorithm as detailed in Appendix C. The lattice volume is chosen to be 128×128 .

Figure 4.2 reports the fermionic correlator as a function of m_q . One can see that a bigger bare quark mass results in a quicker decay, according to the decay law

$$\lim_{t \rightarrow \infty} \langle \psi(t) \bar{\psi}(t) \rangle_{s,s'} \propto e^{-m_{\text{phys}} t}. \quad (4.2)$$

On the other side, a smaller mass results in a slower decay and tends to deform the characteristic shape of the correlator.

Figure 4.3 shows the number of iterations needed for convergence of the Conjugate Gradient algorithm. While the exact number depends on the desired tolerance, one can clearly see that the number of iterations grows as $m_q \rightarrow 0$, due to an increase in the condition number [81] in the Dirac operator.

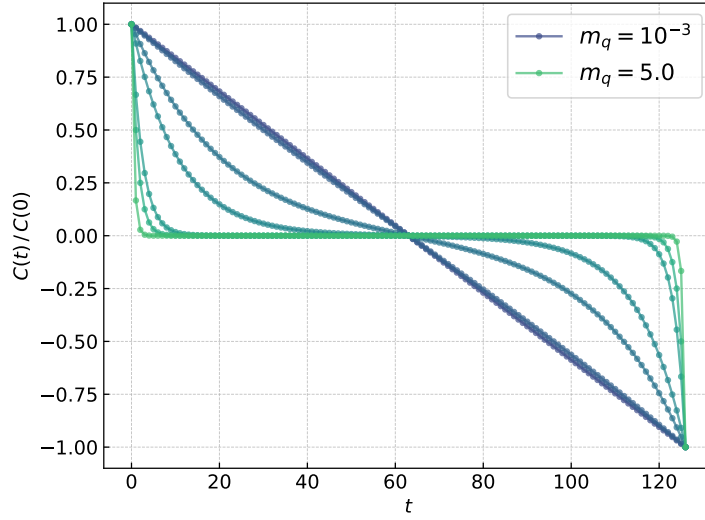


FIGURE 4.2: Normalised fermionic correlator for different values of the bare quark mass. A bigger mass results in a quicker decay of the correlator.

In the case of free Wilson fermions, one can derive an analytical expression for the physical mass, the pole of the propagator [19].

To do this, let us consider the momentum space expression of the Dirac operator, which is derived in Appendix B

$$\bar{D}(p) = \hat{m}_q + \sum_{\mu} 2 \sin^2 \left(\frac{p_{\mu} a}{2} \right) + i \sum_{\mu} \gamma_{\mu} \sin(p_{\mu} a).$$

This can be straightforwardly inverted to

$$\bar{D}^{-1}(p) = \frac{\hat{m}_q + \sum_{\mu} 2 \sin^2 \left(\frac{p_{\mu} a}{2} \right) - i \sum_{\mu} \gamma_{\mu} \sin(p_{\mu} a)}{\left[\hat{m}_q + \sum_{\mu} 2 \sin^2 \left(\frac{p_{\mu} a}{2} \right) \right]^2 + \sum_{\mu} \sin^2(p_{\mu} a)}.$$

One can now find the pole by imposing the denominator evaluated at $p^{\mu} = (im_{\text{phys}}, 0)$ to zero:

$$\left[\hat{m}_q + \sum_{\mu} 2 \sin^2 \left(\frac{p_{\mu} a}{2} \right) \right]_{p_{\mu}=(im_{\text{phys}},0)}^2 + \left[\sum_{\mu} \gamma_{\mu} \sin(p_{\mu} a) \right]_{p_{\mu}=(im_{\text{phys}},0)}^2 = 0.$$

This results in a transcendental equation

$$\left[\hat{m}_q - 2 \sinh^2 \left(\frac{\hat{m}_{\text{phys}}}{2} \right) \right]^2 - \sinh^2(\hat{m}_{\text{phys}}) = 0,$$

which has the solution

$$\hat{m}_{\text{phys}} = \log(1 + \hat{m}_q). \quad (4.3)$$

We then choose three values of the bare quark mass, compute the correlator numerically and perform a fit according to (3.20), in order to extract the physical mass. We

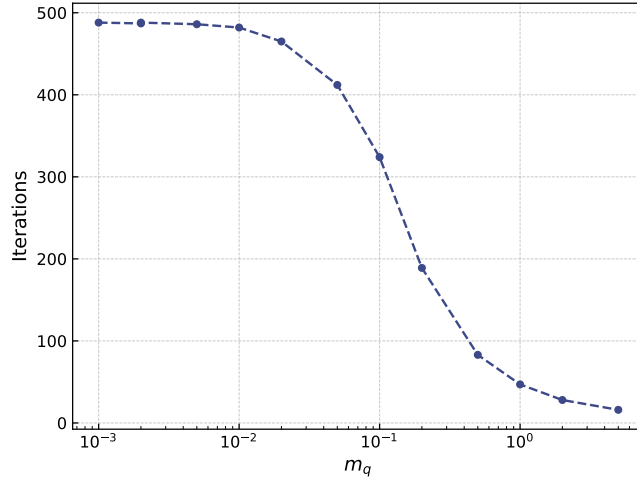


FIGURE 4.3: Conjugate Gradient algorithm iterations as a function of the bare quark mass. As $m_q \rightarrow 0$ the number of iterations grows due to an increase in the condition number.

then compare it to the theoretical value given by (4.3). The results are reported in Figures 4.4 and Table 4.1.

Note that in an interacting theory, excited states are, strictly speaking, negligible only for $t \rightarrow \infty$. This means that they may affect the characteristic shape of the correlator, and one has to either consider only a smaller window centered around $t = N_t/2$, or to make a fit to a portion of the exponential decay, in order to extract the mass. A quantitative method to analyse which interval of the correlator is suitable to make a fit is the so called effective mass [21]

$$m_{\text{eff}}(t + 1/2) = \log \left(\frac{C(t+1)}{C(t)} \right). \quad (4.4)$$

In fact, when the correlator is dominated by the ground state of the system, the effective mass exhibits a plateau at $m_{\text{eff}} = m_{q, \text{phys}}$ as a consequence of the decay law (4.2). One can then either fit the effective mass to a constant value or fit the corresponding interval in the correlator to an exponential decay. An example of fitting procedure for the interacting theory is shown in Figure 4.5.

By fitting the effective mass to a constant we find

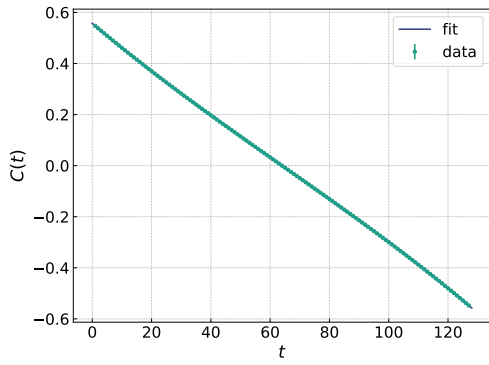
$$m_{q, \text{phys}} = 0.7166243912 \pm 7 \cdot 10^{-10}.$$

By fitting the correlator in the region highlighted by a plateau in the effective mass we find

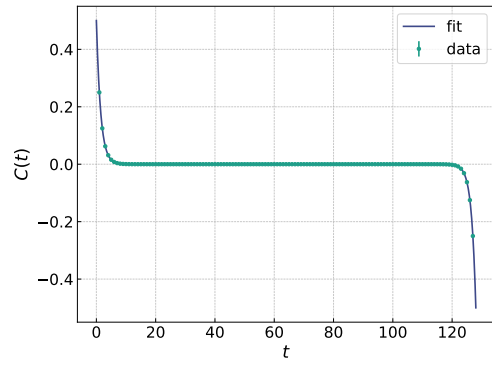
$$m_{q, \text{phys}} = 0.71662602 \pm 2 \cdot 10^{-8}.$$

m_q	Theoretical	Measured
1.0	0.6931471805599453	0.6931537171644739
0.1	0.09531017980432493	0.09531020915059212
0.01	0.009950330853168092	0.009950277657505842

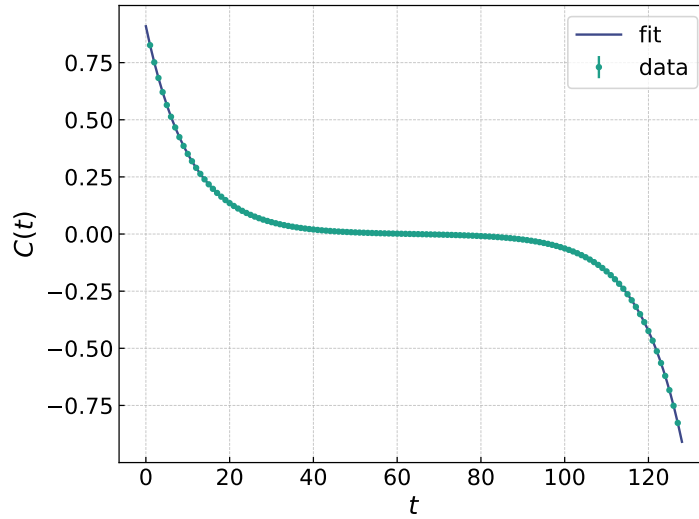
TABLE 4.1: The correlator for free Wilson fermions is fitted to equation (3.20) and compared to its analytical value given by (4.3). The precision for the Conjugate Gradient algorithm was set to $r^2 \leq 10^{-10}$.



(A) Bare quark mass $m_q = 0.01$



(B) Bare quark mass $m_q = 1.0$



(C) Bare quark mass $m_q = 0.1$

FIGURE 4.4: Fit of the free Wilson fermions correlator according to equation (3.20), for three different values of the bare quark mass. The results are reported in Table 4.1.

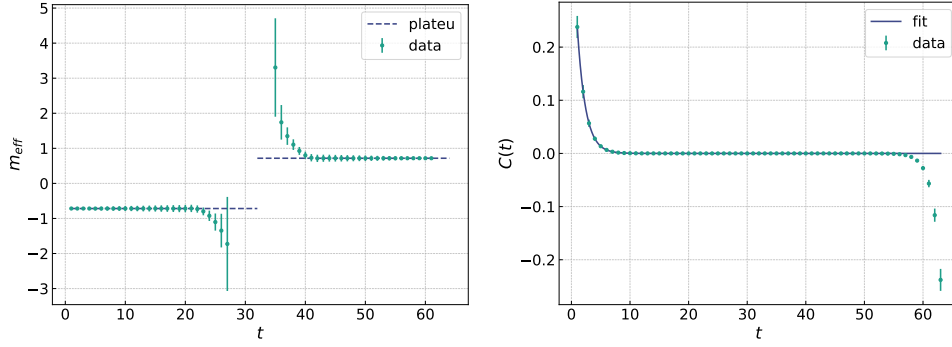


FIGURE 4.5: (Left) Effective mass computed via equation (4.4). The plateau at $m_{\text{eff}} = m_{q,\text{phys}}$ shows the interval in which the correlator is dominated by the ground state of the system. (Right) Correlator in the interacting theory. The interval highlighted by the plateau in the effective mass is fitted to the exponential decay law (4.2).

$$m_\phi^2 = -0.5, \lambda = 1.0, g = 0.2, m_q = 0.8, \text{ Lattice size } 64 \times 64.$$

The correlator was averaged over $\mathcal{O}(5 \cdot 10^4)$ Monte Carlo samples.

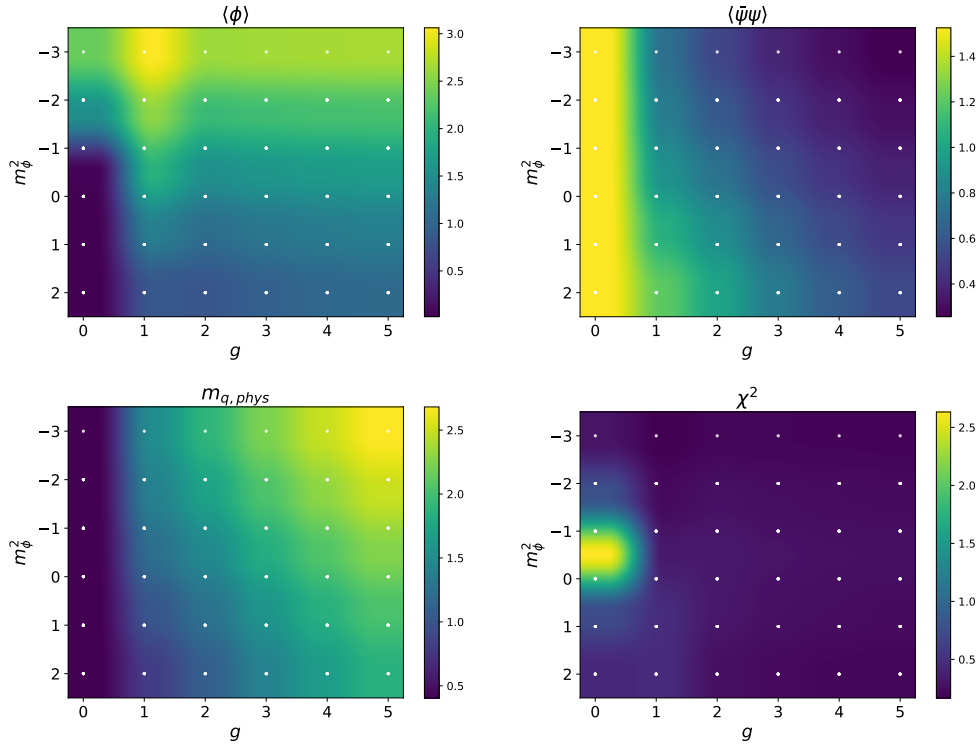


FIGURE 4.6: Slice of the phase diagram at fixed $\lambda = 2.0$. The white dots indicate where data was taken. All the other values have been interpolated. Lattice size 32×32 , $N_{\text{conf}} = \mathcal{O}(10^4)$.

4.3 Phase structure of the Yukawa theory

We want to start the analysis of the Yukawa theory by doing a parameter scan, in order to have a global picture of the phase diagram in the presence of Wilson fermions. For the remainder of this section we set the value of the fermionic bare mass to $m_q = 1.0$.

Figure 4.6 reports a slice of the phase diagram in the $g - m_\phi^2$ plane.

For $g = 0$, the fermionic and bosonic theories are independent. In particular the scalar theory reduces to a $O(1)$ interacting theory: for $m_\phi^2 > 0$ the system lies in a symmetric state identified by $\langle \phi \rangle = 0$. As the mass squared goes to negative values, the scalar field gains a non-zero expectation value, signaling the spontaneous breaking of the $O(1)$ symmetry.

When a finite Yukawa coupling is added, the finite bare quark mass and the Wilson term that break chiral symmetry explicitly, influence the scalar field, which gains a vacuum expectation value due to the relation (2.26). The plot of the chiral condensate shows that chiral symmetry is always broken in the model, even for $g = 0$. Because of this, for $g \neq 0$, one can never speak of a proper phase transition. Thus, one still has a smooth crossover between the two phases. This fact is reflected in the plot of the magnetic susceptibility, which peaks around $m_\phi^2 = 0$ only for small values of g .

As explained in Section 2.5, the presence of a background scalar field can be interpreted as a bare quark mass. This is reflected in the plot of $m_{q,phys}$ which resembles the one of $\langle \phi \rangle$, except for $g = 0$, since the two theories are disconnected.

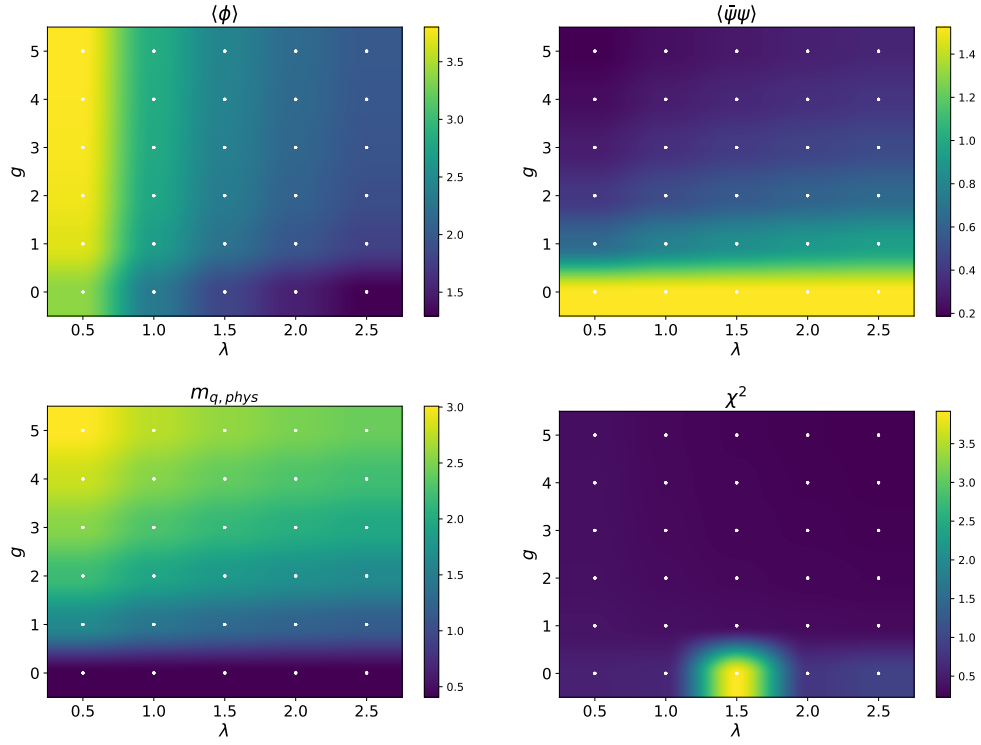


FIGURE 4.7: Slice of the phase diagram at fixed $m_\phi^2 = -1.0$. The white dots indicate where data was taken. All the other values have been interpolated. Lattice size 32×32 , $N_{\text{conf}} = \mathcal{O}(10^4)$.

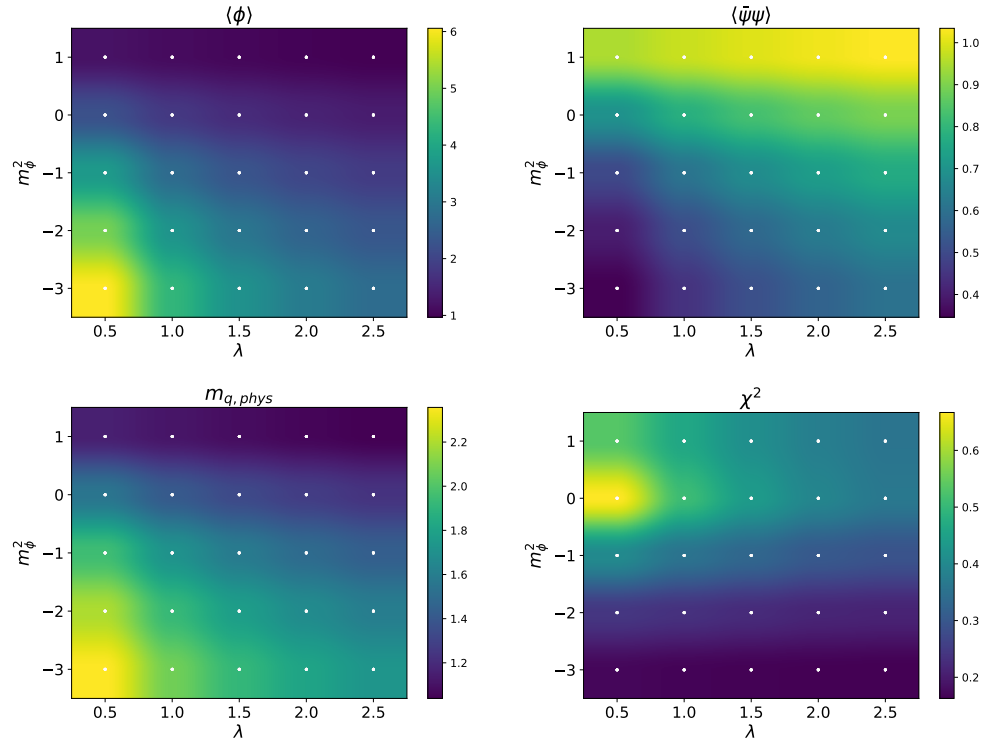


FIGURE 4.8: Slice of the phase diagram at fixed $g = 1.5$. The white dots indicate where data was taken. All the other values have been interpolated. Lattice size 64×64 , $N_{\text{conf}} = \mathcal{O}(10^4)$.

Figure 4.7 reports the phase diagram in the $\lambda - g$ plane. The behavior can be understood qualitatively by means of classical arguments. For $g = 0$, one expects a field magnetisation of order

$$v = \sqrt{-\frac{6m_\phi^2}{\lambda}}.$$

Hence, as λ is increased, the expectation value of the field is reduced. If $g \neq 0$, the fermion mass and the Wilson term contributions increase the expectation value of the field, which in turn works as an additional bare quark mass, hence increasing $m_{q,\text{phys}}$. The behavior of the susceptibility is analogous to the previous case: only if $g = 0$ one has a proper phase transition, reflected in the single peak. The precise value of λ at which this happens depends, mainly, on the choice of m_ϕ^2 .

Finally, let us give a look at the phase structure in the $\lambda - m_\phi^2$ plane. Since here one always has $g \neq 0$, the expectation value of the scalar field and the chiral condensate are never zero, since the symmetry is broken independently of the choice of m_ϕ^2 and λ . This fact is also reflected in the mass plot, where one can clearly see that $m_{q,\text{phys}}$ is always proportional to the scalar field.

Moreover, the susceptibility in this case does not show a single peak as the phase transition can only happen for $g = 0$. Note in fact the difference in magnitude with respect to Figures 4.6 and 4.7.

Chapter 5

Numerical investigation: coloured noise

5.1 Classical-to-quantum interpolation

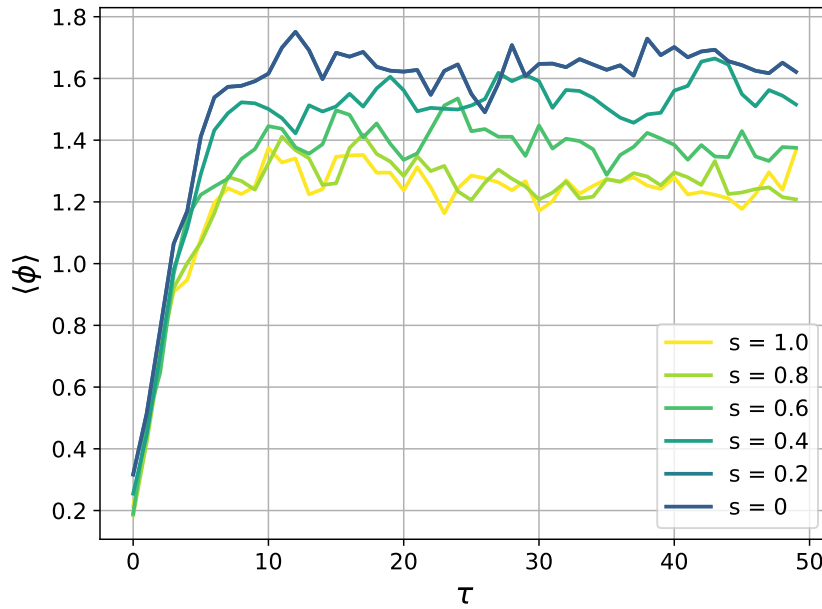


FIGURE 5.1: Thermalisation of the system for different values of the noise fraction s . As noise is added, the equilibrium state of the system shifts accordingly. Coloured noise allows for a smooth interpolation between the fully classical and fully quantum picture. τ indicates the Langevin time evolution from the initial configuration. Lattice size 64×64 , $m_\phi^2 = -1.0$, $\lambda = 0.5$, $g = 0.08$, $m_q = 0.5$.

Let us start by analysing the coloured noise field in the simulation and relevant properties that emerge from it. We consider the Yukawa model described by the continuum action (2.17) and its discrete version (3.5), (3.6).

The system is initialised in the same state for all the configurations on a 64×64 lattice. We consider a simulation with $s = 1$ and then progressively lower the cutoff fraction s , keeping fixed all the quantities in the classical action.

Figure 5.1 shows the system thermalisation for different values of s , namely the Langevin evolution from the initial state to equilibrium. The blue line corresponds to the case $s = 0$, a classical simulation, while the yellow line corresponds to the $s = 1$, the fully quantum case. All the parameters settings are reported under the

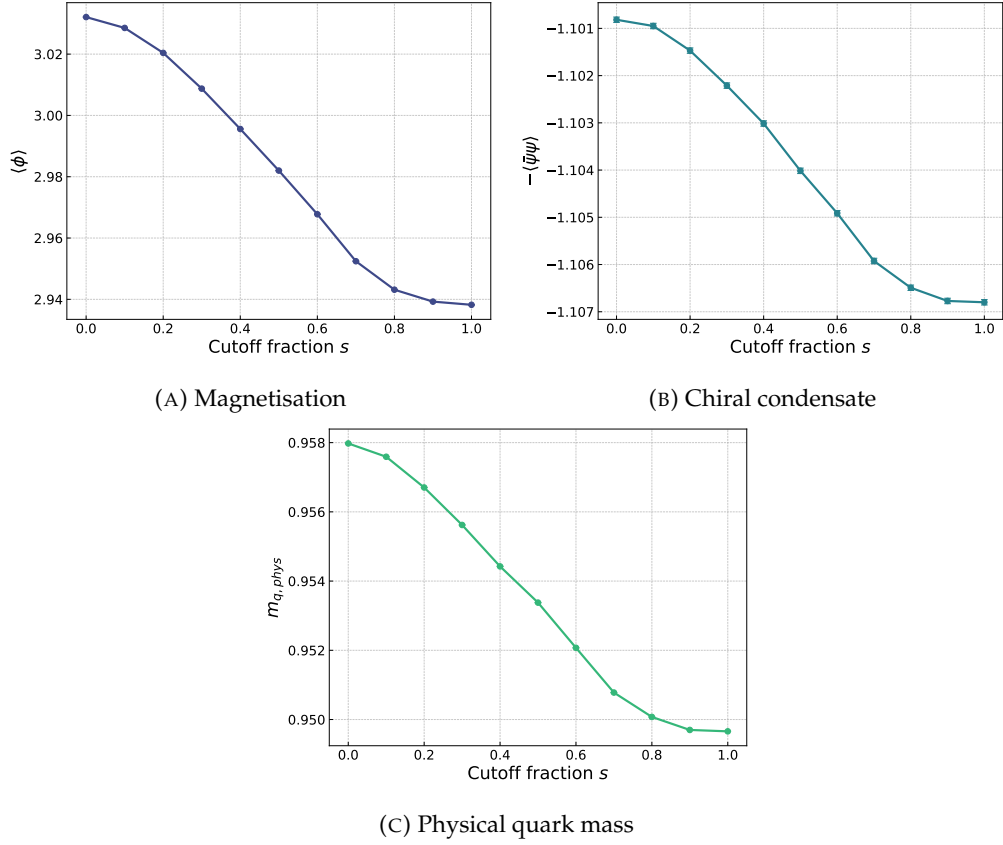


FIGURE 5.2: Relation between magnetisation, chiral condensate and mass, which was motivated in Section 2.5. $m_\phi^2 = -1.0$, $\lambda = 0.7$, $g = 0.2$, $m_q = 1.0$. Lattice size 64×64 , $N_{\text{conf}} = \mathcal{O}(5 \cdot 10^4)$.

figure. As quantum modes are removed via coloured noise, the system shifts its equilibrium point.

We now want to make use of coloured noise to understand the relation between scalar field, quark condensate and fermionic mass, which was qualitatively discussed in Section 2.5 by means of classical arguments.

Keeping all the parameters fixed, we perform simulations changing the value of the cutoff fraction s , and we measure the three quantities mentioned above: the results are reported in Figure 5.2. One can clearly see that as quantum modes are added, one has

$$\langle\phi\rangle \sim \langle\bar{\psi}\psi\rangle \sim m_q.$$

This makes clear at first that the scalar field ϕ effectively plays the role of quark bilinear in the dynamics. Moreover, the physical mass of the quark grows proportionally to the scalar field magnetisation at all levels in the quantum theory.

The interconnection of these phenomena is an important result if one interprets it in the context of effective theories. In fact, often in QCD, the dynamical chiral symmetry breaking mechanism is described by low energy Yukawa-type effective models such as Gross-Neveu, Nambu – Jona-Lasinio or Quark Meson, to name some examples, where a scalar field emerges after a Hubbard-Stratonovich transformation [82].

5.2 Chiral fermions and noise-induced transition

As explained in Section 2.5, chiral symmetry can be broken, in the continuum theory, either explicitly via the introduction of a finite bare quark mass, or spontaneously if the field gains a non-zero expectation value.

Moreover, in the discrete formulation, the introduction of the Wilson term contributes to the explicit breaking of chiral symmetry, as shown in Appendix B. This, in particular, means that chiral symmetry is explicitly broken also for $m_q \rightarrow 0$. Because of this, one needs a new definition of the bare mass M_q , which takes into account the Wilson term contribution, such that chiral symmetry is restored in the limit $M_q \rightarrow 0$. In a lattice study of a theory such as two-flavours QCD, what one typically does [20, 21] is the following: the spontaneous breaking of chiral symmetry generates three goldstone massless bosons, the pions. If the bare quark mass is zero, the physical mass of the pions has to be zero, as a consequence of Goldstone's theorem [83]. Hence one can measure the pion masses and find a value m_q^* such that when $m_q \rightarrow m_q^*$, one has $m_\pi \rightarrow 0$.

This approach is not feasible in our theory, since it is described by a discrete chiral symmetry, and no Goldstone modes appear as a consequence. A possible way of proceeding [84] could be to tune the bare quark mass as a function of the interaction couplings in order to set the renormalised mass to zero, causing a divergence of the correlation length. In this case, the physical quantities of interest become independent of the underlying lattice, and one expects to recover the desired continuum QFT. A discussion on the issue, together with other proposals for the definition of the bare quark mass for similar theories can be found in [85, 86]. We do not follow such approaches here, mostly because of time limits, but also because it is not our purpose to match any precise model, but rather investigate properties of the coloured noise technique. In this section we just consider naïve fermions, and the chiral limit is reached for $m_q \rightarrow 0$. Thus, one has to keep in mind that due to the fermion doubling this represents a theory with $2N_f = 4$ degenerate quarks.

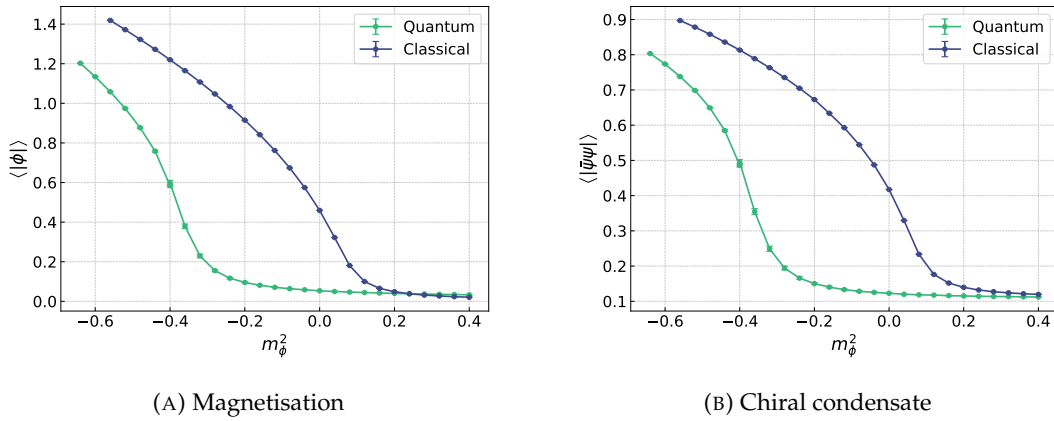


FIGURE 5.3: Scalar mass scan of the quantum and classical theories. One can see that for values of scalar squared mass $-0.2 \leq m_\phi^2 \leq 0$, the classical and the quantum systems lie in two different phases. $\lambda = 1.951, g = 0.08$. Lattice size 32×32 , $N_{\text{conf}} = \mathcal{O}(10^4)$.

In Figure 5.3, the (absolute) magnetisation and the chiral condensate are studied as a function of the bosonic mass squared, both in the fully quantum and fully classical theory. One can notice that the classical system undergoes a phase transition at values of m_ϕ^2 bigger than the quantum counterpart.

Note that as the bare quark mass is small but finite, this is not a proper phase transition and the latter will be, eventually, reached in the limit $m_q \rightarrow 0$.

We then pick a value $m_\phi^2 = -0.123$. Using coloured noise, we then interpolate between the classical and quantum pictures for different values of the quark mass, namely $m_q = 10^{-2}, 5 \cdot 10^{-3}, 10^{-3}$.

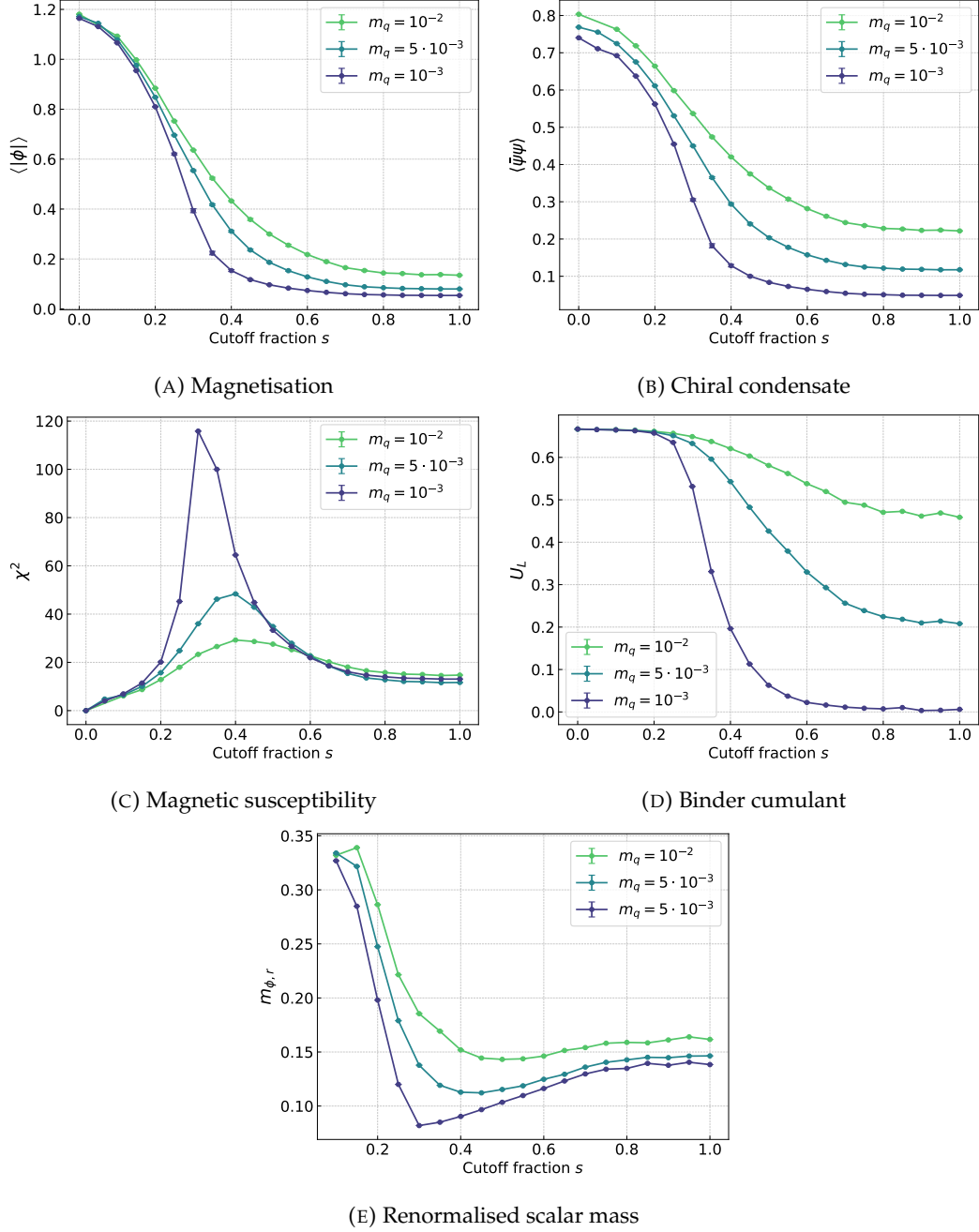


FIGURE 5.4: Noise-induced transition. The classical theory lies in the broken phase, while the symmetry is restored in the quantum theory.

$$m_\phi^2 = -0.123, \lambda = 1.951, g = 0.08.$$

$$\text{Lattice size } 64 \times 64, N_{\text{conf}} = \mathcal{O}(5 \cdot 10^4).$$

One can clearly see in Figure 5.4 that as the quark mass is lowered the difference between the two phases gets more pronounced, indicating a phase transition. Both the magnetisation and the chiral condensate are finite in the classical theory

and get washed out as quantum fluctuations are added. The peak in the susceptibility shows the transition is happening for $s \approx 0.3$, but the resolution is not enough to determine the precise value of.

The Binder parameters assumes the value $U_L = 0$ in the symmetric phase, and $U_L = 2/3$ in the broken phase, as expected. Finally, the scalar renormalised mass tends to zero as the transition point is approached, signaling the divergence of the correlatin length.

Hence all the five observables are in agreement and signal the presence of a phase transition.

Intuitively speaking, one can interpret the situation by looking at Figure 2.4. For $m_\phi^2 < 0$, the classical potential has two minima that are slightly inequivalent due to the presence of a small Yukawa coupling. In the classical theory, the system is constrained at the global minimum, since there is no stochasticity and the kinetic term is not strong enough to cause the hopping between the two minima. At the quantum level, fluctuations allow such transition bringing $\langle \phi \rangle \rightarrow 0$ and restoring the symmetry. Note that in order to confirm that a phase transition took place, one should first consider $V \rightarrow \infty$ and then $m_q \rightarrow 0$. If the order parameters of the classical and quantum theories still indicates that the system is in two different phases, one can draw that conclusion.

In this context, it would be interesting to look at the physical quark mass. In fact, neglecting the bare quark mass $m_q \approx 0$, one would expect the fermions to be massive in the classical theory due to the presence of the background field ϕ , which works as an additional mass. In the classical-to-quantum transition, as the field expectation vanishes, the fermions become massless. Thus, due to the choice of discretisation, namely employing naïve fermions, it is not possible to extract the quark mass in a straightforward way due to the properties of the doublers. The latter exhibits in fact a wrong sign in the momentum dispersion relation [87, 88].

5.3 Cooling with coloured noise

Let us now consider one of the main applications of coloured noise, namely the cooling technique.

We first set up a white noise simulation with $s = 1$, and then progressively lower s . The lowering of the cutoff is compensated by a change in the couplings, as explained in Section 3.3. We study the behaviour of the system both as a function of the bosonic mass squared m_ϕ^2 and the Yukawa coupling g . A summary of the parameters choice for both the experiments is reported in tables 5.1 and 5.2.

s	N_t	N_x	m_ϕ^2	λ	g	m_q	K_ψ
1	16	16	m_ϕ^2	0.4	0.3	0.5	K_ψ
1/2	32	32	$m_\phi^2/4$	0.1	0.3	0.5	$K_\psi/4$
1/4	64	64	$m_\phi^2/16$	0.025	0.3	0.5	$K_\psi/16$
1/8	128	128	$m_\phi^2/64$	0.00625	0.3	0.5	$K_\psi/64$

TABLE 5.1: Parameter settings in the cooling procedure for the bosonic mass squared scan. Each coupling in the bosonic action is rescaled according to its canonical dimension, while the fermionic sector rescaling is implemented directly at the drift level, as detailed in Section 3.3.

s	N_t	N_x	m_ϕ^2	λ	g	m_q	K_ψ
1	16	16	0.5	0.7	g	1.0	K_ψ
1/2	32	32	0.125	0.175	g	1.0	$K_\psi/4$
1/4	64	64	0.0625	0.04375	g	1.0	$K_\psi/16$
1/8	128	128	0.03125	0.001094	g	1.0	$K_\psi/64$

TABLE 5.2: Parameters setting in the cooling procedure for the Yukawa coupling scan. Each coupling in the bosonic action is rescaled according to its canonical dimension, while the fermionic sector rescaling is implemented directly at the drift level, as detailed in Section 3.3.

Figure 5.5 reports the magnetisation, its susceptibility and the chiral condensate as a function of the bare scalar mass squared m_ϕ^2 , while Figure 5.6 reports the investigation as a function of the Yukawa coupling. One can clearly see that there is a general good agreement for the first three block-spin transformations, even if based on tree level arguments.

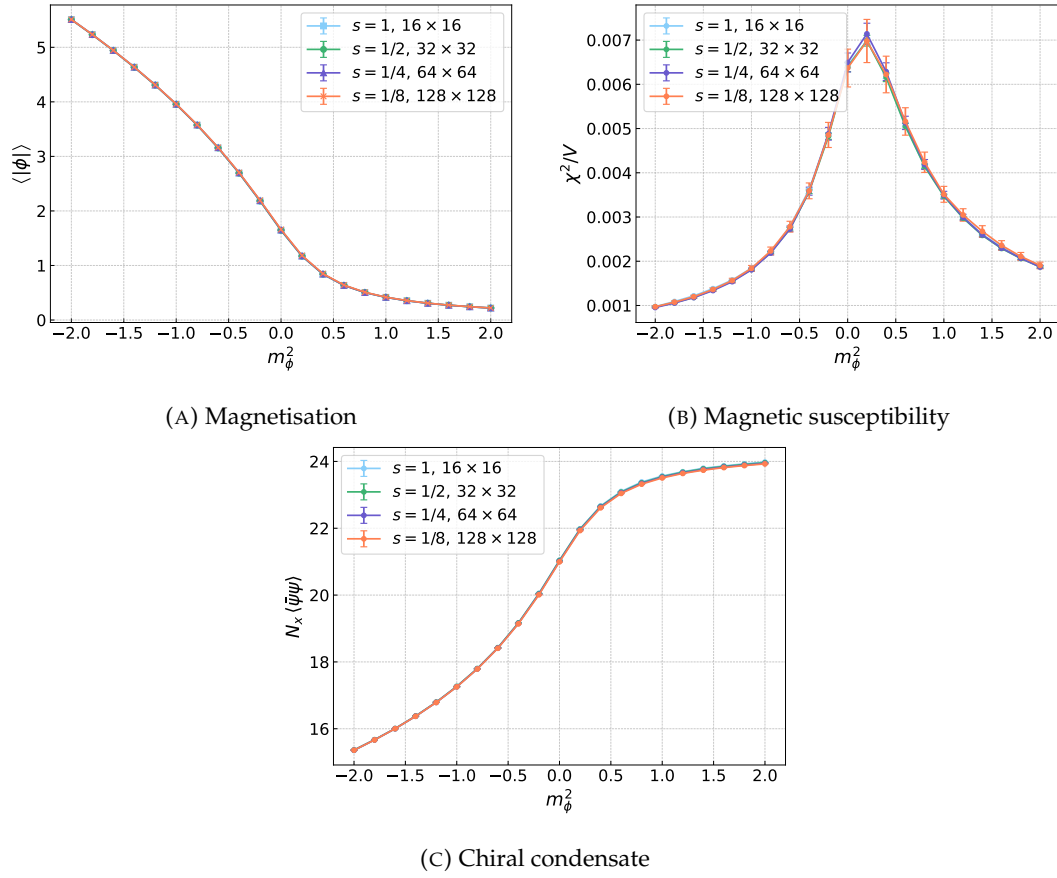


FIGURE 5.5: Cooling via coloured noise. The absolute magnetisation, its susceptibility and the chiral condensate are compared after performing block-spins transformations as a function of the bosonic mass squared. All the parameters are reported in Table 5.1.

$$N_{\text{conf}} = \mathcal{O}(5 \cdot 10^4).$$

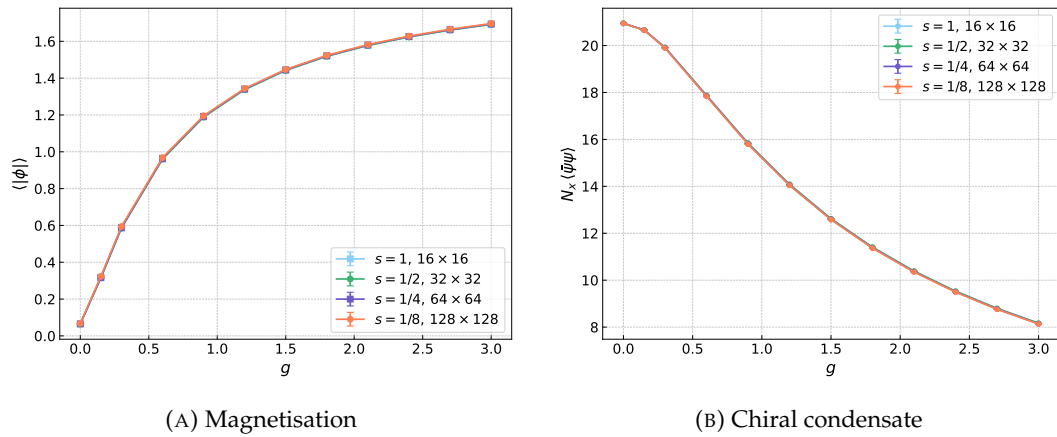


FIGURE 5.6: Cooling via coloured noise. The absolute magnetisation and the chiral condensate are compared after performing block-spins transformations as a function of the Yukawa coupling.

All the parameters are reported in Table 5.2.

$$N_{\text{conf}} = \mathcal{O}(5 \cdot 10^4).$$

The most relevant observables are the magnetisation and the chiral condensate, since they are the order parameters of the theory. We therefore want to provide a more detailed comparison of the performance of the procedure. To this end we define the relative errors

$$\begin{aligned}\epsilon_\phi(s) &= \frac{\langle |M| \rangle_s - \langle |M| \rangle}{\langle |M| \rangle}, \\ \epsilon_\psi(s) &= \frac{N_x^{(s)} \langle |\bar{\psi} \hat{\psi}| \rangle_s - N_x \langle |\bar{\psi} \hat{\psi}| \rangle}{N_x \langle |\bar{\psi} \hat{\psi}| \rangle}.\end{aligned}\quad (5.1)$$

The deviations quantified by such parameters is reported in Figure 5.7 and Figure 5.8.

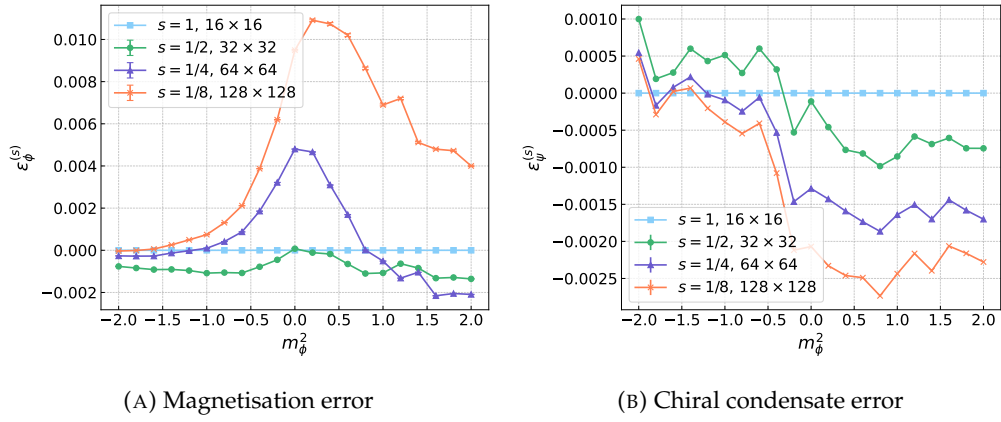


FIGURE 5.7: Relative error of the absolute magnetisation and chiral condensate in the cooling procedure as a function of the scalar mass squared m_ϕ^2 , for various values of the noise fraction s .

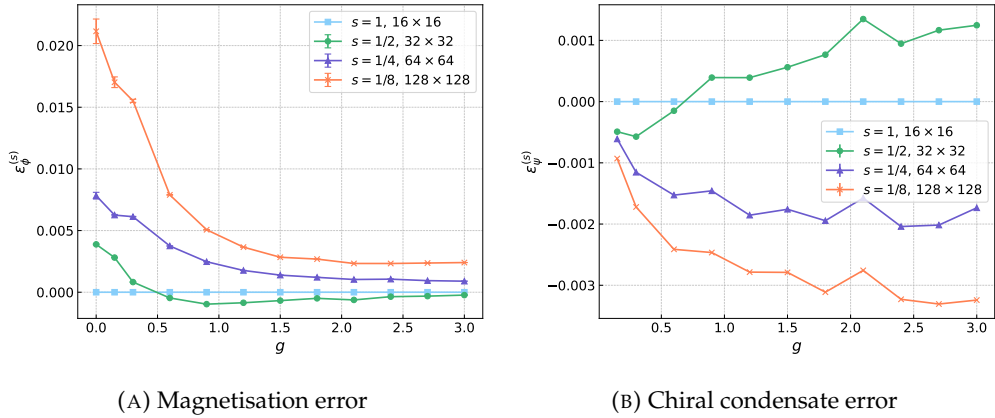


FIGURE 5.8: Relative error of the absolute magnetisation and chiral condensate in the cooling procedure as a function of the Yukawa coupling g , for various values of the noise fraction s .

Errors obviously increase with successive iterations, since the approximations are multiple.

First of all, a tree level rescaling neglects coupling momentum dependencies which do not stem from spacetime rescaling; the assumption is thus justified for high

enough cutoffs.

Moreover, the assumption that any change due to a modification of the cutoff can be absorbed by a redefinition of the couplings is itself non-trivial. In fact, following a Wilsonian RG perspective, as momentum shells are integrated out, all the relevant operators, including those not present in the classical action, grow as the cutoff is lowered. As before, the assumption is justified for high enough cutoffs. A quantitative analysis on this aspect was done in [66], where a procedure to systematically test until when it is possible to accommodate the cutoff change by a redefinition of the couplings was proposed, eventually including also beyond tree level transformations.

Finally, we also want to look at more complex observables such as the fermionic physical mass and the bosonic renormalised mass. They are reported in Figure 5.9 and Figure 5.10.

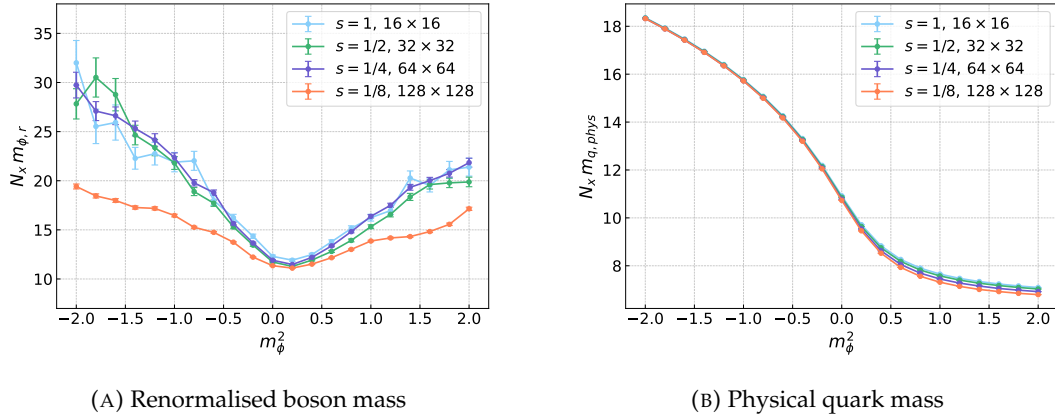


FIGURE 5.9: Renormalised bosonic mass $m_{\phi,r}$ and pole fermionic mass $m_{q,phys}$ for various values of the noise fraction s .

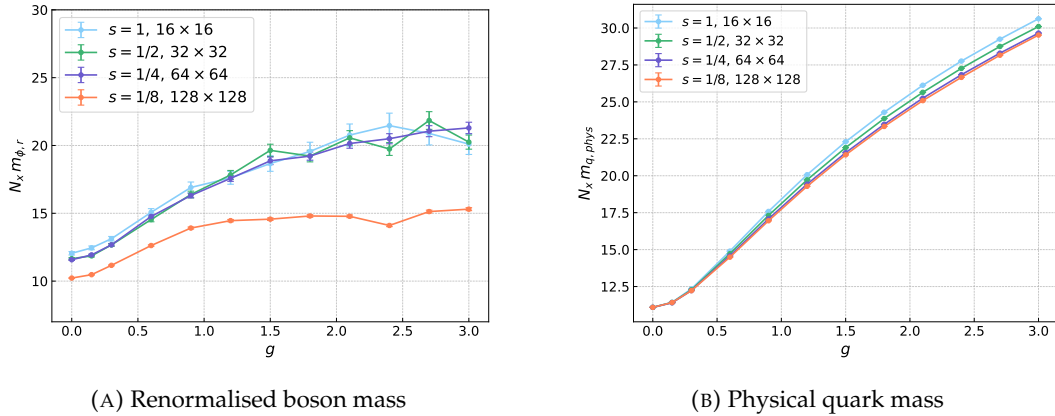


FIGURE 5.10: Renormalised bosonic mass $m_{\phi,r}$ and pole fermionic mass $m_{q,phys}$ for various values of the noise fraction s .

As one can see, there is a clear deviation for $m_{\phi,r}$ at the third block-spin iteration. This is indeed a delicate issue that resides in the use of sharp cutoffs to regulate the noise term. In fact, as shown in Section 2.3.2, the noise-to-noise correlation function expressed in momentum space exhibits an oscillating behaviour described by a Bessel function, which was calculated and shown in Figure 2.3.

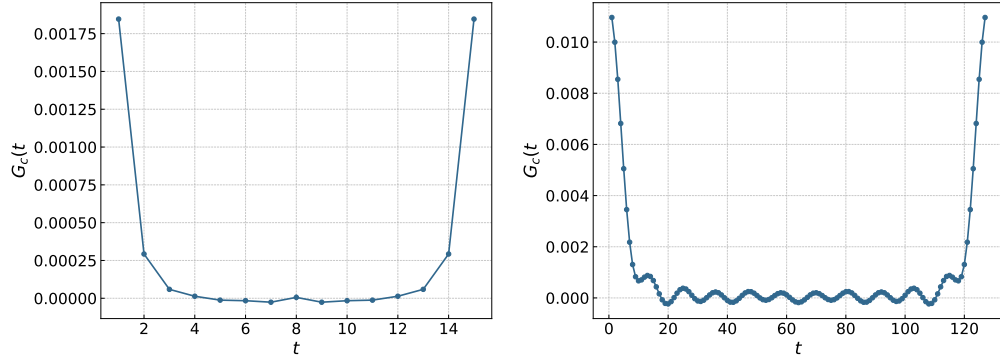


FIGURE 5.11: (Left) Connected two-point function of the original theory on the 16×16 lattice. (Right) Connected two-point function after three block spin-iterations at cutoff fraction $s = 1/8$, on a 128×128 lattice. The use of the sharp cutoff as a regulating function results in a disturbance of the signal of the bosonic two-point function. The Bessel function profile which was shown in Figure 2.3 induces errors in the calculation of the renormalised mass.

As a consequence, correlation functions are affected by this behaviour. This holds particularly for the connected two-point function as shown in Figure 5.11. This explains the big discrepancy encountered in the renormalised mass in Figures 5.9 and 5.10. This error cannot be solved by simply going to higher order correction to the rescaling procedure, but can only be fixed by changing the regulating term, since it is an intrinsic characteristic of the latter.

For what concerns the physical quark mass, which also shows some discrepancy, further investigation is needed to understand the cause of the problem.

Another source of error is the following: since the regulating term applies, strictly speaking, only to the noise term, after performing a block-spin transformation the quantum theory is set back at its original scale, while the classical one lies at a finer spacing.

Even with the presence of these problems, it is nevertheless remarkable that observables such as the order parameters are not significantly altered in the coarse-graining procedure.

Chapter 6

Summary and outlook

Summary

In this thesis stochastic quantisation with coloured noise was introduced as a framework to control the momentum dependency of quantum fluctuations in a lattice field theory simulation.

Chapter 2 and Chapter 3 were devoted to the introduction of the relevant theoretical aspects and methodologies for this work. In particular, the formulation of stochastic quantisation in the presence of coloured noise resulted in a deep connection with the Wilsonian (functional) renormalisation group.

We then turned to the numerical analysis and experiments, applying the technique to a fermionic theory, a Yukawa model. In Chapter 4, a preliminary analysis was carried out. The phase diagram of the theory showed that a proper phase transition in the model can happen only for vanishing Yukawa interaction due to the presence of Wilson fermions, which break chiral symmetry explicitly. Nevertheless, relevant features of the model such as the relation between magnetisation, chiral condensate, and fermionic mass, could be investigated.

After switching momentarily to the formulation with naïve fermions, removing the Wilson term, the behavior of the system in the presence of different noise degrees of freedom was studied and it was shown that for a particular combination of the bare parameters a phase transition can happen while smoothly interpolating between the classical and quantum theories.

Finally, it was shown how the simulation can be cooled from ultraviolet degrees of freedom by encoding them in a redefinition of the bare couplings, performing block-spin transformations. It was shown that observables such as the magnetisation, chiral condensate, and magnetic susceptibility are not significantly altered in the coarse-graining procedure. Other observables such as the scalar renormalised mass and fermionic pole mass, were shown to present some problems in the procedure. While the cause for the former has been elucidated and attributed to the choice of the regulating function for the noise term, more investigation is needed to understand the cause of the latter.

Outlook

The main result of this work is that the coarse-graining procedure via block-spin transformations was successfully applied to a fermionic theory. This adds another step towards a bigger goal, namely taking the continuum limit of a lattice low-energy effective theory such as the Quark-Meson model. This would not only allow for a comparison between lattice results and functional methods, but would also remove the undesired effects of the Wilson term in the action. An interesting step forward starting from this work, would be to extend the investigation to systems at finite temperature and chemical potential. This could have particular benefits in lattice algorithms such as the Complex Langevin method, which aim at beating the sign problem, and often rely on cooling techniques for stabilisation.

An application of the algorithm to gauge theories would also be of great interest since the cooling procedure could then be applied to simulations of full QCD. In particular, we mention that an application in Yang-Mills theories could allow for a connection with the Wilson gradient flow of gauge links and allow for a precise control of the latter. Thus, this would be quite harder due to the fact that a momentum space cutoff breaks the gauge invariance of the theory.

Acknowledgements

At this point, I would like to thank Jan Pawłowski for the opportunity to work on this project in the group of Strongly Correlated Systems, as well as for the guidance and general supervision in the course of the last year.

I am grateful to Thomas Gasenzer, for accepting to be the co-advisor of this thesis.

Many thanks to Felipe Attanasio, for the continuous and invaluable technical help over the last year, and for his guidance in the jungle of GPU programming.

I am grateful also to the Heidelberg Institute for Theoretical Physics (ITP) and Baden-Württemberg computing facilities for the computational resources, without which this project would have not been possible.

Thanks to Luca, Alessandro, Davide, Javier, and Heinrich for proof-reading this thesis, and contributing to the outcome.

Finally, thanks to my family and all of my friends for the support and encouragement given in these years.

Matteo Zortea

Appendix A

Conventions

Spinor representation

We choose the following representation of the two-dimensional γ matrices

$$\gamma_0 = \sigma_3 = \begin{pmatrix} 1 & 0 \\ 0 & -1 \end{pmatrix}, \quad \gamma_1 = \sigma_1 = \begin{pmatrix} 0 & 1 \\ 1 & 0 \end{pmatrix}.$$

They satisfy the Euclidean Clifford algebra

$$\{\gamma_\mu, \gamma_\nu\} = 2\delta_{\mu,\nu},$$

and they have the following properties

$$\gamma_\mu^\dagger = \gamma_\mu, \quad \gamma_\mu^2 = \mathbb{1}.$$

We then introduce γ_5 as

$$\gamma_5 = i\gamma_0\gamma_1 = \begin{pmatrix} 0 & i \\ -i & 0 \end{pmatrix},$$

with the following properties

$$\gamma_5^\dagger = \gamma_5, \quad \gamma_5^2 = \mathbb{1}, \quad \{\gamma_5, \gamma_\mu\} = 0.$$

Fourier transform

The Fourier transformation of a function $f : \mathbb{R}^d \rightarrow \mathbb{R}$ is given by

$$\bar{f}(p) = \mathcal{F}[f](p) = \int_x e^{-ixp} f(x),$$

and its inverse is

$$f(x) = \mathcal{F}^{-1}[\bar{f}](x) = \frac{1}{(2\pi)^d} \int_p e^{ixp} \bar{f}(p).$$

Appendix B

Wilson fermions

The naïve discretisation of the fermionic action for free fermions yields the Dirac operator components

$$\hat{D}_{nm} = \sum_{\mu} \gamma_{\mu} \frac{\delta_{n,n+\mu} - \delta_{n,n-\mu}}{2} + m_q \delta_{nm} ,$$

which have the momentum representation

$$\hat{D} = \hat{m}_q + i \sum_{\mu} \gamma_{\mu} \sin(p_{\mu} a) .$$

The last expression can be easily inverted

$$\hat{D}^{-1}(p) = \frac{\hat{m}_q - i \sum_{\mu} \gamma_{\mu} \sin(p_{\mu} a)}{\hat{m}_q^2 + \sum_{\mu} \sin^2(p_{\mu} a)} .$$

For $m_q = 0$, one can easily see that, in addition to $\hat{p}_{\mu} = 0$, all the edges of the Brillouin zone $\hat{p}_{\mu} \in \{\pm\pi/a, \pm\pi/a\}$ are poles. They indeed represent additional fermions, which come from the discretisation of the action. These additional degrees of freedom are called doublers and represent unphysical particles, at least if one's goal is to recover the original continuum theory. If m_q is finite,

The idea proposed by Wilson to remove the doublers is to redefine the action as

$$S_W = S - \frac{r}{2} \sum_{m,n} \hat{\psi}(m) \hat{\square} \hat{\psi}(n) ,$$

where

$$\left(\hat{\square}\right)_{mn} = \sum_{\mu} \frac{\delta_{m,n+\hat{\mu}} + \delta_{m,n-\hat{\mu}} - 2\delta_{mn}}{2} ,$$

and $r \in [0, 1]$ is a free parameter. In this project we always consider $r = 1$.

The Wilson-Dirac operator assumes the form

$$\hat{D} = \hat{m}_q + \sum_{\mu} \gamma_{\mu} \frac{\delta_{m,m+\hat{\mu}} - \delta_{m,m-\hat{\mu}}}{2} + \frac{r}{2} \sum_{\mu} \frac{\delta_{m,n+\hat{\mu}} + \delta_{m,n-\hat{\mu}} - 2\delta_{mn}}{2} .$$

and its momentum space representation is

$$\begin{aligned}
 \hat{D}(p) &= \hat{m}_q + i \sum_{\mu} \gamma_{\mu} \sin(p_{\mu} a) + \frac{r}{2} \sum_{\mu} [\cos(p_{\mu} a) - 1] \\
 &= \hat{m}_q + i \sum_{\mu} \gamma_{\mu} \sin(p_{\mu} a) + r \sum_{\mu} \frac{\cos(p_{\mu} a) - 1}{2} \\
 &= \hat{m}_q + i \sum_{\mu} \gamma_{\mu} \sin(p_{\mu} a) + r \sum_{\mu} \sin^2\left(\frac{p_{\mu} a}{2}\right).
 \end{aligned}$$

The last expression can be inverted straightforwardly

$$\begin{aligned}
 \hat{D}^{-1}(p) &= \frac{\hat{m}_q + \frac{2r}{a} \sum_{\mu} \sin^2(p_{\mu} a/2) - i \sum_{\mu} \gamma_{\mu} \sin(p_{\mu} a)}{\left[\hat{m}_q + \frac{2r}{a} \sum_{\mu} \sin^2(p_{\mu} a/2)\right]^2 + \sum_{\mu} \sin^2(p_{\mu} a)} \\
 &= \frac{\hat{M}(p) - i \sum_{\mu} \gamma_{\mu} \sin(p_{\mu} a)}{\hat{M}^2(p) + \sum_{\mu} \sin^2(p_{\mu} a)},
 \end{aligned}$$

where we defined $\hat{M}(p) \equiv \hat{m}_q + \frac{2r}{a} \sum_{\mu} \sin^2(p_{\mu} a/2)$.

For every $\hat{p}_{\mu} \neq (\pm\pi/a, \pm\pi/a)$, one has that $a \rightarrow 0$ implies $\hat{M}(p) \rightarrow \hat{m}_q$.

Instead, for every momentum vector that lies at the edge of the Brillouin zone $M(p) \rightarrow \infty$ as $a \rightarrow 0$. This removes the fermion doublers in the continuum limit.

A notable problem is that one then loses chiral symmetry since the Wilson term is clearly not invariant under neither the continuous transformation

$$\psi \rightarrow e^{i\theta\gamma_5} \psi, \quad \bar{\psi} \rightarrow -\bar{\psi} e^{i\theta\gamma_5},$$

nor the discrete

$$\psi \rightarrow \gamma_5 \psi, \quad \bar{\psi} \rightarrow -\bar{\psi} \gamma_5.$$

It is in fact proven that one either completely removes the doublers or breaks chiral symmetry [68].

Appendix C

Computational strategies

The application of coloured noise, and in particular the cooling technique, demand for an efficient volume scaling of the simulation, as pointed out in Section 4.1. The code for this project was developed accordingly.

While a full documentation of the code esulates from the scope of this thesis, we want to provide some details on the strategies that were adopted.

The code for this project has been developed to run on a Graphical Processing Unit (GPU). This ensures a massive parallelisation for operations such as scalar products and reduction operations such as summing components of a vector, which are extensively used in the course of the project.

Choice of the spinor basis

The choice of the chiral basis for the spinors illustrated in Appendix A was done for computational performance purposes. To see this, one has to look at the explicit expression of the Wilson projectors in the chiral basis:

$$\begin{aligned}\Gamma_{-\hat{0}} &= (1 + \gamma_0) = \begin{bmatrix} 2 & 0 \\ 0 & 0 \end{bmatrix}, & \Gamma_{+\hat{0}} &= (1 - \gamma_0) = \begin{bmatrix} 0 & 0 \\ 0 & 2 \end{bmatrix}, \\ \Gamma_{-\hat{1}} &= (1 + \gamma_1) = \begin{bmatrix} 1 & 1 \\ 1 & 1 \end{bmatrix}, & \Gamma_{+\hat{1}} &= (1 - \gamma_1) = \begin{bmatrix} 1 & -1 \\ -1 & 1 \end{bmatrix}.\end{aligned}$$

Note that all the matrices are degenerate. This implies that when the Wilson projectors are applied to a vector, only half of the components have to be computed, and the other can be deduced since they are either zero or linearly dependent. Explicitly:

$$\begin{aligned}(1 - \gamma_0) \psi(n + \hat{0}) &= \begin{bmatrix} 0 & 0 \\ 0 & 2 \end{bmatrix} \begin{bmatrix} \psi_1 \\ \psi_2 \end{bmatrix} = \begin{bmatrix} 0 \\ 2\psi_2 \end{bmatrix}, \\ (1 + \gamma_0) \psi(n - \hat{0}) &= \begin{bmatrix} 2 & 0 \\ 0 & 0 \end{bmatrix} \begin{bmatrix} \psi_1 \\ \psi_2 \end{bmatrix} = \begin{bmatrix} 2\psi_1 \\ 0 \end{bmatrix}, \\ (1 - \gamma_1) \psi(n + \hat{1}) &= \begin{bmatrix} 1 & -1 \\ -1 & 1 \end{bmatrix} \begin{bmatrix} \psi_1 \\ \psi_2 \end{bmatrix} = \begin{bmatrix} \psi_1 - \psi_2 \\ -\psi_1 + \psi_2 \end{bmatrix} \equiv \begin{bmatrix} \eta \\ -\eta \end{bmatrix}, \\ (1 + \gamma_1) \psi(n - \hat{1}) &= \begin{bmatrix} 1 & 1 \\ 1 & 1 \end{bmatrix} \begin{bmatrix} \psi_1 \\ \psi_2 \end{bmatrix} = \begin{bmatrix} \psi_1 + \psi_2 \\ \psi_1 + \psi_2 \end{bmatrix} \equiv \begin{bmatrix} \chi \\ \chi \end{bmatrix}.\end{aligned}$$

Inverting the Dirac operator

One can note that for the purpose of computing the fermionic contribution to the drift force and the extraction of the physical quark mass from the correlator (details in Section 3.2 and Section 3.4), we do not need the full inverse of the Dirac operator, but only the inverse matrix applied to a vector. Hence it is sufficient to compute

$$\psi = D^{-1} \eta. \quad (\text{C.1})$$

Computing ψ via equation (C.1) is equivalent to solve the linear system $D\psi = \eta$, which can be done efficiently by employing a method for sparse matrices such as Conjugate Gradient (CG) as explained in the following way.

We want to solve the equation

$$D\psi = \eta.$$

CG requires the matrix to be hermitian while D is only γ^5 -hermitian, namely

$$\gamma_5 D \gamma_5 = D^\dagger.$$

One can thus solve the linear system

$$(DD^\dagger) \xi = \eta,$$

and then obtain ψ by multiplying the solution ξ by D^\dagger since

$$D^\dagger \xi = D^\dagger (DD^\dagger)^{-1} \eta = D^{-1} \eta = \psi. \quad (\text{C.2})$$

Analogously, one can calculate

$$\chi = (D^\dagger)^{-1} \eta$$

by solving

$$(D^\dagger D) \xi = \eta,$$

and then applying D to the result.

Bilinear noise scheme

When computing the drift for the Langevin evolution, one needs to evaluate the trace of the Dirac operator, as shown in Section 3.2.

We compute the trace by employing the bilinear noise scheme. For this, one needs a set of N vectors of normally distributed random complex numbers, namely vectors η_i where each component η_i^α satisfies

$$\langle \eta_i^\alpha \rangle = 0, \quad \langle \eta_i^\alpha \eta_j^\beta \rangle = \delta_{ij} \delta^{\alpha\beta}.$$

The trace of the matrix is then computed as

$$\text{Tr } A = \frac{1}{N} \lim_{N \rightarrow \infty} \sum_i^N \eta_i^\dagger A_{ij} \eta_j. \quad (\text{C.3})$$

In our case, since $A = D^{-1}$, we can first compute

$$\psi = D^{-1} \eta = D^\dagger \underbrace{(DD^\dagger)^{-1}}_{\text{CG}} \eta$$

by means of the Conjugate Gradient algorithm, and then obtain the trace as

$$\text{Tr } A = \eta^\dagger \psi.$$

Not that the series (C.3) requires in principle an infinite number of vectors to evaluate the trace exactly. In practice we truncate it to $N = 1$. The average over Monte Carlo samples will eventually converge nevertheless to the right result in the limit of infinite samples.

Bibliography

- [1] K. G. Wilson, "Confinement of quarks," *Phys. Rev. D*, **10**, pp. 2445–2459, 8 1974.
- [2] J. Greensite, "An Introduction to the Confinement Problem." 2011, vol. 821.
- [3] A. Masayuki and Y. Koichi, "Chiral restoration at finite density and temperature," *Nuclear Physics A*, **504**, no. 4, pp. 668–684, 1989.
- [4] M. Stephanov, K. Rajagopal, and E. Shuryak, "Signatures of the tricritical point in qcd," *Physical Review Letters*, **81**, no. 22, pp. 4816–4819, 1998.
- [5] J. Berges and K. Rajagopal, "Color superconductivity and chiral symmetry restoration at non-zero baryon density and temperature," *Nuclear Physics B*, **538**, no. 1–2, pp. 215–232, 1999.
- [6] F. Wilczek, "Application of the renormalization group to a second-order qcd phase transition," *International Journal of Modern Physics A*, **07**, no. 16, pp. 3911–3925, 1992.
- [7] G. Endrödi, "Qcd phase diagram: Overview of recent lattice results," *Journal of Physics: Conference Series*, **503**, no. 1, p. 012 009, 2014.
- [8] R. D. Pisarski and D. H. Rischke, "Gaps and critical temperature for color superconductivity," *Phys. Rev. D*, **61**, p. 051 501, 5 2000.
- [9] M. Alford, K. Rajagopal, and F. Wilczek, "Qcd at finite baryon density: Nucleon droplets and color superconductivity," *Physics Letters B*, **422**, no. 1–4, pp. 247–256, 1998.
- [10] B. C. Barrois, "Superconducting quark matter," *Nuclear Physics B*, **129**, no. 3, pp. 390–396, 1977.
- [11] W.-j. Fu, J. M. Pawłowski, and F. Rennecke, "Qcd phase structure at finite temperature and density," *Phys. Rev. D*, **101**, p. 054 032, 5 2020.
- [12] B. C. Barrois, "Superconducting quark matter," *Nuclear Physics B*, **129**, no. 3, pp. 390–396, 1977.
- [13] F. Gao and J. M. Pawłowski, "Chiral phase structure and critical end point in qcd," *Physics Letters B*, **820**, p. 136 584, 2021.
- [14] S. Borsanyi *et al.*, "Qcd crossover at finite chemical potential from lattice simulations," *Phys. Rev. Lett.*, **125**, p. 052 001, 5 2020.
- [15] A. Bazavov *et al.*, "Chiral crossover in qcd at zero and non-zero chemical potentials," *Physics Letters B*, **795**, pp. 15–21, 2019.
- [16] O. Philipsen, "Lattice constraints on the qcd chiral phase transition at finite temperature and baryon density," *Symmetry*, **13**, no. 11, 2021.
- [17] M. A. Stephanov, "Qcd phase diagram: An overview," 2006.
- [18] R. Bellwied *et al.*, "The qcd phase diagram from analytic continuation," *Physics Letters B*, **751**, pp. 559–564, 2015.
- [19] I. Montvay and G. Münster, "Quantum Fields on a Lattice." 1994.

- [20] H. J. Rothe, "Lattice Gauge Theories," 4th. WORLD SCIENTIFIC, 2012.
- [21] C. Gattringer and C. B. Lang, "Lattice quantum chromodynamics."
- [22] M. Creutz, "Quarks, Gluons and Lattices." Cambridge University Press, 2023.
- [23] K. G. Wilson, "Confinement of quarks," *Phys. Rev. D*, **10**, pp. 2445–2459, 8 1974.
- [24] U.-J. Wiese, "An introduction to lattice field theory," 2009.
- [25] G. Aarts and I.-O. Stamatescu, "Stochastic quantization at finite chemical potential," *Journal of High Energy Physics*, **2008**, no. 09, p. 018, 2008.
- [26] C. Berger, L. Rammelmüller, A. Loheac, F. Ehmman, J. Braun, and J. Drut, "Complex langevin and other approaches to the sign problem in quantum many-body physics," *Physics Reports*, **892**, pp. 1–54, 2021.
- [27] E. Seiler, "Status of complex langevin," *EPJ Web of Conferences*, **175**, p. 01 019, 2018.
- [28] G. Aarts, E. Seiler, and I.-O. Stamatescu, "Complex langevin method: When can it be trusted?" *Physical Review D*, **81**, no. 5, 2010.
- [29] F. Attanasio, G. Aarts, B. Jaeger, and D. Sexty, "Results on the heavy-dense QCD phase diagram using complex Langevin," *PoS, LATTICE2016*, p. 074, 2017.
- [30] F. Attanasio, B. Jäger, and F. P. G. Ziegler, "Complex langevin simulations and the qcd phase diagram: Recent developments," *The European Physical Journal A*, **56**, no. 10, 2020.
- [31] J. Langelage, M. Neuman, and O. Philipsen, "Onset transition to cold nuclear matter from lattice qcd with heavy quarks to κ^4 ," 2013.
- [32] D. K. Sinclair and J. B. Kogut, "Complex langevin for lattice qcd at $T = 0$ and $\mu \geq 0$," 2016.
- [33] D. Sexty, "Simulating full qcd at nonzero density using the complex langevin equation," *Physics Letters B*, **729**, pp. 108–111, 2014.
- [34] G. Aarts, "Introductory lectures on lattice qcd at nonzero baryon number," *Journal of Physics: Conference Series*, **706**, p. 022 004, 2016.
- [35] G. Aarts, F. A. James, J. M. Pawłowski, E. Seiler, D. Sexty, and I.-O. Stamatescu, "Stability of complex langevin dynamics in effective models," *Journal of High Energy Physics*, **2013**, no. 3, 2013.
- [36] E. Seiler, D. Sexty, and I.-O. Stamatescu, "Gauge cooling in complex langevin for lattice qcd with heavy quarks," *Physics Letters B*, **723**, no. 1–3, pp. 213–216, 2013.
- [37] K. G. Wilson, "Renormalization group and critical phenomena. i. renormalization group and the kadanoff scaling picture," *Phys. Rev. B*, **4**, pp. 3174–3183, 9 1971.
- [38] K. G. Wilson, "Renormalization group and critical phenomena. ii. phase-space cell analysis of critical behavior," *Phys. Rev. B*, **4**, pp. 3184–3205, 9 1971.
- [39] K. G. Wilson and J. Kogut, "The renormalization group and the ϵ expansion," *Physics Reports*, **12**, no. 2, pp. 75–199, 1974.
- [40] Y. Nambu and G. Jona-Lasinio, "Dynamical model of elementary particles based on an analogy with superconductivity. i," *Physical Review*, **122**, no. 1, 1961.

- [41] Y. Nambu and G. Jona-Lasinio, "Dynamical model of elementary particles based on an analogy with superconductivity. II," *Physical Review*, **124**, no. 1, 1961.
- [42] D. J. Gross and A. Neveu, "Dynamical symmetry breaking in asymptotically free field theories," *Phys. Rev. D*, **10**, pp. 3235–3253, 10 1974.
- [43] L. Shen, J. Berges, J. M. Pawłowski, and A. Rothkopf, "Thermalization and dynamical spectral properties in the quark-meson model," *Physical Review D*, **102**, no. 1, 2020.
- [44] B.-J. Schaefer and J. Wambach, "The phase diagram of the quark–meson model," *Nuclear Physics A*, **757**, no. 3–4, pp. 479–492, 2005.
- [45] N. Tetradis, "The quark–meson model and the phase diagram of two-flavour qcd," *Nuclear Physics A*, **726**, no. 1–2, pp. 93–119, 2003.
- [46] L. D. Landau, "On the theory of phase transitions," *Zh. Eksp. Teor. Fiz.*, **7**, pp. 19–32, 1937.
- [47] V. L. Ginzburg, "On superconductivity and superfluidity (what i have and have not managed to do), as well as on the 'physical minimum' at the beginning of the 21st century," *ChemPhysChem*, **5**, no. 7, pp. 930–945, 2004.
- [48] "Conceptual foundations of quantum field theory. Proceedings, Symposium and Workshop, Boston, USA, March 1-3, 1996," Cambridge, UK: CUP, 1999.
- [49] A. C. Hewson and J. Kondo, "Kondo effect," *Scholarpedia*, **4**, p. 7529, 2009.
- [50] L. P. Kadanoff, "Scaling laws for ising models near T_c ," *Physics Physique Fizika*, **2**, pp. 263–272, 6 1966.
- [51] K. G. Wilson and M. E. Fisher, "Critical exponents in 3.99 dimensions," *Phys. Rev. Lett.*, **28**, pp. 240–243, 4 1972.
- [52] J. Cardy, "The renormalization group idea," *Scaling and Renormalization in Statistical Physics*. Cambridge University Press, 1996, pp. 28–60.
- [53] M. E. Peskin and D. V. Schroeder, "An Introduction to quantum field theory." Reading, USA: Addison-Wesley, 1995.
- [54] A. Carosso, "Novel approaches to renormalization group transformations in the continuum and on the lattice," 2020.
- [55] J. Berges, N. Tetradis, and C. Wetterich, "Non-perturbative renormalization flow in quantum field theory and statistical physics," *Physics Reports*, **363**, no. 4–6, pp. 223–386, 2002.
- [56] J. Polonyi, "Lectures on the functional renormalization group method," *Open Physics*, **1**, no. 1, pp. 1–71, 2003.
- [57] J. M. Pawłowski, "Aspects of the functional renormalisation group," *Annals of Physics*, **322**, no. 12, pp. 2831–2915, 2007.
- [58] B. Delamotte, "An introduction to the nonperturbative renormalization group," *Lecture Notes in Physics*. Springer Berlin Heidelberg, 2012, pp. 49–132.
- [59] O. J. Rosten, "Fundamentals of the exact renormalization group," *Physics Reports*, **511**, no. 4, pp. 177–272, 2012.
- [60] M. Le Bellac, "Thermal Field Theory." Cambridge University Press, 1996.
- [61] E. Seiler, "The case against asymptotic freedom," 2003.

- [62] S. Friedli and Y. Velenik, “Statistical Mechanics of Lattice Systems: A Concrete Mathematical Introduction.” Cambridge University Press, 2017.
- [63] G. Parisi and Y.-S. Wu, “Perturbation theory without gauge fixing,” *Scientia Sinica*, p. 483, 24 1981.
- [64] P. H. Damgaard and H. Hüffel, “Stochastic quantization,” *Physics Reports*, **152**, no. 5-6, pp. 227–398, 1987.
- [65] C. Gardiner, “Stochastic Methods: A Handbook for the Natural and Social Sciences.” Springer Berlin, Heidelberg, 2009, pp. XVIII, 447.
- [66] J. M. Pawłowski, I. O. Stamatescu, and F. P. Ziegler, “Cooling stochastic quantization with colored noise,” *Physical Review D*, **96**, no. 11, 2017.
- [67] M. Schwartz, “Quantum Field Theory and the Standard Model.” 2013.
- [68] H. Nielsen and M. Ninomiya, “Absence of neutrinos on a lattice: (i). proof by homotopy theory,” *Nuclear Physics B*, **185**, no. 1, pp. 20–40, 1981.
- [69] P. H. Ginsparg and K. G. Wilson, “A remnant of chiral symmetry on the lattice,” *Phys. Rev. D*, **25**, pp. 2649–2657, 10 1982.
- [70] N. D. Mermin and H. Wagner, “Absence of ferromagnetism or antiferromagnetism in one- or two-dimensional isotropic heisenberg models,” *Phys. Rev. Lett.*, **17**, pp. 1133–1136, 22 1966.
- [71] A. Ayala, L. A. Hernández, M. Loewe, and C. Villavicencio, “QCD phase diagram in a magnetized medium from the chiral symmetry perspective: the linear sigma model with quarks and the Nambu–Jona-Lasinio model effective descriptions,” 2021.
- [72] A. Manohar and H. Georgi, “Chiral quarks and the non-relativistic quark model,” *Nuclear Physics B*, **234**, no. 1, pp. 189–212, 1984.
- [73] G. G. Batrouni, G. R. Katz, A. S. Kronfeld, G. P. Lepage, B. Svetitsky, and K. G. Wilson, “Langevin simulations of lattice field theories,” *Phys. Rev. D*, **32**, pp. 2736–2747, 10 1985.
- [74] A. S. Kronfeld, “Dynamics of Langevin simulations,” *Prog. Theor. Phys. Suppl.*, **111**, pp. 293–312, 1993.
- [75] V. V. Williams, Y. Xu, Z. Xu, and R. Zhou, “New bounds for matrix multiplication: From alpha to omega,” 2023.
- [76] H. Avron and S. Toledo, “Randomized algorithms for estimating the trace of an implicit symmetric positive semi-definite matrix,” *J. ACM*, **58**, no. 2, 2011.
- [77] W. Horsthemke, “Noise induced transitions,” *Non-Equilibrium Dynamics in Chemical Systems*, Berlin, Heidelberg: Springer Berlin Heidelberg, 1984, pp. 150–160.
- [78] R. Toral, “Noise-induced transitions vs. noise-induced phase transitions,” *AIP Conference Proceedings*, **1332**, no. 1, pp. 145–154, 2011.
- [79] F. Attanasio, J. P. Klinger, and J. M. Pawłowski, “Low energy effective theories on the lattice with coloured noise,” 2022.
- [80] K. Binder and D. Heermann, “Monte Carlo Simulation in Statistical Physics: An Introduction.” Springer Berlin Heidelberg, 2010.
- [81] Y. Saad, “Iterative Methods for Sparse Linear Systems,” Second. Society for Industrial and Applied Mathematics, 2003.
- [82] J. Hubbard, “Calculation of partition functions,” *Phys. Rev. Lett.*, **3**, pp. 77–78, 2 1959.

- [83] J. Goldstone, A. Salam, and S. Weinberg, "Broken symmetries," *Phys. Rev.*, **127**, pp. 965–970, 3 1962.
- [84] A. Bermudez, E. Tirrito, M. Rizzi, M. Lewenstein, and S. Hands, "Gross–neveu–wilson model and correlated symmetry-protected topological phases," *Annals of Physics*, **399**, pp. 149–180, 2018.
- [85] Y. Iwasaki, "Phase diagram of QCD at finite temperatures with Wilson fermions," *Nucl. Phys. B Proc. Suppl.*, **42**, pp. 96–102, 1995.
- [86] L. Maiani and G. Martinelli, "Current algebra and quark masses from a monte carlo simulation with wilson fermions," *Physics Letters B*, **178**, no. 2, pp. 265–271, 1986.
- [87] Y. Cohen, S. Elitzur, and E. Rabinovici, "A monte carlo study of the gross-neveu model," *Nuclear Physics B*, **220**, no. 1, pp. 102–118, 1983.
- [88] J. Lenz, L. Pannullo, M. Wagner, B. Wellegehausen, and A. Wipf, "Inhomogeneous phases in the gross-neveu model in $1 + 1$ dimensions at finite number of flavors," *Phys. Rev. D*, **101**, p. 094512, 9 2020.

List of Figures

1.1	The phase diagram of QCD	1
2.1	Block-spin transformation	6
2.2	The Wilsonian renormalisation group	8
2.3	Correlated noise	13
2.4	Classical potential and symmetry breaking	18
3.1	Temperatures on the lattice	24
4.1	Computational complexity of the Conjugate Gradient algorithm. . . .	32
4.2	Fermionic correlator	33
4.3	Conjugate Gradient algorithm iterations as a function of the bare quark mass.	34
4.4	Fit of the correlator for free Wilson fermions.	35
4.5	Effective mass	36
4.6	Phase diagram in the $g - m_\phi^2$ plane	37
4.7	Phase diagram in the $\lambda - g$ plane	38
4.8	Phase diagram in the $\lambda - m_\phi^2$ plane	38
5.1	Thermalisation of the system for different values of the noise fraction s	41
5.2	Relation between magnetisation, condensate and mass	42
5.3	Scalar mass scan of the quantum and classical theories	43
5.4	Noise-induced transition	44
5.5	Cooling stochastic quantisation: fields as a function of the bosonic mass squared.	47
5.6	Cooling stochastic quantisation: fields as a function of the Yukawa coupling.	47
5.7	Relative error in the cooling procedure at tree level as a function of the scalar mass squared.	48
5.8	Relative error in the cooling procedure at tree level as a function of the Yukawa coupling.	48
5.9	More observables in the cooling procedure as a function of the scalar mass squared	49
5.10	More observables in the cooling procedure as a function of the Yukawa coupling	49
5.11	Effect of the sharp cutoff on the connected two-point function	50

List of Tables

4.1	Fit of the correlator for free Wilson fermions.	35
5.1	Parameter settings in the cooling procedure for the bosonic mass squared scan	46
5.2	Parameter settings in the cooling procedure for the Yukawa coupling scan.	46

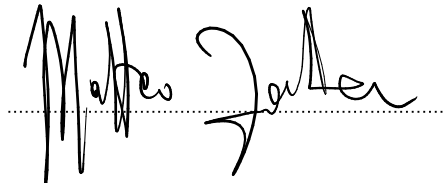
List of Abbreviations

RG	R enormalisation G roup
fRG	F unctional R enormalisation G roup
UV	U ltraviolet
IR	I nfrared
QFT	Q uantum F ield T heory
QCD	Q uantum C hromodynamics
NJL	N ambu – J ona- L asinio
CG	C onjugate G radient

Erklärung:

Ich versichere, dass ich diese Arbeit selbstständig verfasst habe und keine anderen als die angegebenen Quellen und Hilfsmittel benutzt habe.

Heidelberg, den 27.11.2023

A handwritten signature in black ink, reading "Matteo Zeller", is written over a horizontal dotted line. The signature is fluid and cursive, with the first name "Matteo" and the last name "Zeller" clearly distinguishable.